



UNIVERSITÀ DI PARMA

ARCHIVIO DELLA RICERCA

University of Parma Research Repository

Experimental study on radial gravity currents flowing in a vegetated channel

This is the peer reviewed version of the following article:

Original

Experimental study on radial gravity currents flowing in a vegetated channel / Petrolo, Diana; Ungarish, Marius; Chiapponi, Luca; Longo, Sandro Giovanni. - In: JOURNAL OF FLUID MECHANICS. - ISSN 1469-7645. - 933:(2022), pp. A46.1-A46.38. [10.1017/jfm.2021.1059]

Availability:

This version is available at: 11381/2906330 since: 2022-01-26T11:09:59Z

Publisher:

Cambridge University Press

Published

DOI:10.1017/jfm.2021.1059

Terms of use:

Anyone can freely access the full text of works made available as "Open Access". Works made available

Publisher copyright

note finali coverpage

(Article begins on next page)

12 August 2025

Experimental study on radial gravity currents flowing in a vegetated channel

¹D. Petrolo,[†] ²M. Ungarish, ¹L. Chiapponi,
¹S. Longo

¹Department of Engineering and Architecture - Università degli Studi di Parma - Parco Area delle Scienze 181/A - 43124 Parma - Italy

²Department of Computer Science, Technion, Israel Institute of Technology, Haifa 32000, Israel

(Received ?; revised ?; accepted ?. - To be entered by editorial office)

We present an experimental study of gravity currents in cylindrical geometry, in the presence of vegetation. Forty tests were performed with a denser volume of fluid (brine advancing in a fresh water ambient fluid) in lock-release, and with a constant and time-varying flow rate, both waxing and waning. The brine was injected or released in the corner of a circular sector tank of angle 30° with radius equal to 180 cm and with two different densities of the vegetation, simulated with vertical plastic rods with diameter $D = 1.6$ cm. The measurements consist of marking the height profile of the current as a function of r and t and the position of the front as a function of t , where r and t are the radius and the time. The results indicate a self-similar structure, with the lateral profiles that after an initial adjustment collapse to a single curve in scaled variables. The propagation of the front is well described by time at a constant power law function. The existence of self-similarity on an experimental basis corroborates a simple theoretical model. The model assumptions are that (i) the dominant balance is between buoyancy and drag, parameterized by a power law of the current velocity $\sim |u|^{\lambda-1}u$; (ii) the current advances in shallow water conditions; (iii) ambient fluid dynamics are negligible. In order to evaluate the value of λ (the only tuning parameter of the theoretical model), we performed two series of measurements with the same two vegetation density values of the tested gravity currents, obtaining λ for different values of the Reynolds number of the rods, which was computed by assuming the diameter of the vegetation stems as length scale. In our tests λ increased from 1 to 2 while Reynolds increased from 100 to approximately $6 \cdot 10^3$. Two further tests with rods with diameter $D = 0.8$ cm and with the same density of the larger rods indicate that drag coefficient and the transition from $\lambda = 1$ to $\lambda = 2$ are quantitatively affected by D , but the structure of the model is not.

The model interprets the tests correctly under all inflow conditions, with a more significant deviation from the experimental results for the waning inflow rate case and for the lateral current profiles only. These results are comforting since, although in most of the tested gravity currents λ varies (typically 30% about the value 1.7) in time and space, a robust self-similar structure of the flow field is maintained.

Key words: gravity currents, vegetation, drag force, experiments.

[†] Email address for correspondence: diana.petrolo@unipr.it

1. Introduction

Gravity currents (GCs) develop whenever there is a density difference between the current fluid, with density ρ_c , and the ambient fluid, with density ρ_a . These currents propagate at the bottom of the ambient fluid when $\rho_c > \rho_a$ (hyperpycnal), or at the top of the ambient fluid in the opposite case (hypopycnal). If the ambient fluid is stratified, currents propagate at the level of equal density (mesopycnal). The current and ambient fluid are not necessarily different, as a difference in density may be related to a difference in temperature or to suspended particles inside the heavier fluid. Many examples of GCs occur in natural environments, such as dust and sand risen from turbulent wind, avalanches of small snow-flakes that grow flowing along the hazardous slopes of mountains, or cold air near the floor of a room coming in from an opened window. More examples can be found in the extensive monographs by Simpson (1999) and Huppert (2006).

GCs are often classified on the basis of the terms that dominate the momentum balance, distinguishing inertial-buoyancy and viscous-buoyancy regimes. In the presence of obstacles or vegetation, the balance can also be turbulent drag-buoyancy. There are several possible sources of turbulent drag; it can be associated with entrainment with the ambient fluid and with the structure of the flow field (see, e.g. Lane-Serff 1993), or with the presence of obstacles spatially extended. The presence of turbulent drag suggests an analogy between GCs flow and flow in Forchheimer regime in porous media (Hatcher *et al.* 2000), with a velocity profile that appears uniform in the vertical and with dissipation controlled by the obstacles, with negligible bottom effects. If the GC can spread over a sufficient space, a transition is expected with the current initially in inertial-buoyancy regime, then in viscous-buoyancy regime depending on the Reynolds number (with the exception of critical GCs, see Maxworthy 1983; Chiapponi *et al.* 2018). In the presence of turbulent drag, a further transition is expected, with inertia initially dominant, then overtaken by turbulent drag and finally replaced by viscous drag.

The behaviour of the stream is conditioned by the release mechanism at the source: a lock-release (LR) consists of a finite volume of current released instantaneously into the environment, whereas a constant-flow or a time-varying flow current is a flow continuously fed from a source at a constant or time-varying flow rate; in the latter case waxing or waning flows rate can be modelled. Many simplifications can be adopted in the models, whether the ratio $\rho_a/\rho_c \approx 1$ or not (Boussinesq and non-Boussinesq currents), or the dynamics of the ambient fluid can be neglected in the propagation characteristics of the current (single layer model). For more details, see the recent comprehensive book by Ungarish (2020).

The great interest in this broad natural phenomenon, and the enormous variety of configurations in the environment and industry, has stimulated a rich line of theoretical and experimental research, with advanced numerical techniques and sophisticated measuring instruments. The simplest configuration, with a horizontal bottom, is perhaps the one most intensively investigated, starting with Benjamin's pioneer publication (Benjamin 1968) with numerous extensions to a general cross-section (Ungarish 2018), and with stratification of the ambient fluid (Longo *et al.* 2016).

More complex models refer to particle-driven currents (Sparks *et al.* 1993; Hogg *et al.* 2000; Zemach *et al.* 2017; Lippert & Woods 2020). Sher & Woods (2017) described the relative importance of entrainment at the interface and particle sedimentation in controlling the run-out distance of short-lived GCs, and the influence of an up-slope boundary has been considered by Ottolenghi *et al.* (2016); Martin *et al.* (2020); De Falco *et al.* (2021). Recent studies (Longo *et al.* 2018; Sciortino *et al.* 2018; Chiapponi *et al.*

2019) have focused on the effects of a free top, such as a superficial depression bounded to the advancing nose; these effects are usually neglected.

In the vast majority of cases, models refer to currents advancing in a confined section with hydraulically smooth walls, or on a smooth bottom. However, almost always ambient GCs interact with obstacles of various kinds, as happens for flows through forests, urban and aquatic canopies, as documented in many reviews (Finnigan 2000; Belcher *et al.* 2012; Nepf 2012). Vegetation-like obstacles are often modelled as flexible or rigid vertical cylinders with diameter D and height h , with h being smaller or larger than the ambient fluid height H , and vegetation is said to be submerged when $h < H$. A relevant parameter is the density of the vegetation, $\kappa = nA_c/A$, defined as the ratio of the plane area occupied by the cylinders, nA_c , to the total area of the lower base of the channel, A , where n is the total number of cylinders and $A_c = \pi D^2/4$ is the cross-sectional area of a single cylinder.

Lock-release GCs in the presence of artificial vegetation (thin flexible plastic tubes) have been studied, e.g. by Naftchali *et al.* (2016), who carried out experiments with κ in the range [0.006, 0.014] and found that for increasing κ the current velocity decreases up to 28.5%, while the density of the current ρ_c decreases up to 82% as a consequence of mixing. When κ is small, any small change in ρ_c does not cause a significant change in the forward velocity of the current. Cenedese *et al.* (2018) (experiments with vertical rigid cylinders) found that when the current height is smaller than the vegetation height, the current front has a triangular shape, but when the current is higher than the vegetation, two different regimes develop for the small (sparse arrays) and large (dense arrays) κ respectively: (i) in the sparse arrays configuration ($\kappa = 0.09$), the denser fluid current propagates between the cylinders with high entrainment enhanced by the vortices generated in the wake of the cylindrical obstacles; (ii) in the dense arrays configuration ($\kappa = 0.35$), the denser fluid current is almost entirely above the vegetation, where the drag force is lower, and undergoes convective instability, mixing vertically with the environment and diluting near the nose.

In more complex situations, vegetation and the presence of shallow water promote density stratification of thermal origin and the onset of a GC. Zhang & Nepf (2008) studied the effects of different heat exchange between the open water and the canopy (they used a random array of rigid, emergent cylinders to represent the canopy region), a configuration with the water within the submerged vegetation absorbing less solar heat than the adjacent deep water. They found that the velocity of the current is reduced by the drag of the canopy in the vegetative region, while in the open region the velocity of the current remains constant and depends only on the initial conditions. Numerical simulations indicate that in both partially and fully vegetated regions, currents are inertial for $C_D \xi_T l_c < 10$, where C_D is the drag coefficient, $\xi_T = nD/A$ is the array density (fraction of the frontal area of cylinders per unit volume where A is the bed area and ξ_T has dimension of L^{-1}), and l_c is the total length of the current, provided that $C_D \xi_T H/n < 13.39$. When $C_D \xi_T H/n > 13.39$, currents are entrained due to the high vegetation density and short inertia flow time period (Tsakiri *et al.* 2016).

Testik & Ungarish (2016) conducted a theoretical analysis on both lock-release and continuous-flow GCs in a rectangular channel in the presence of artificial vegetation (cylindrical rods), comparing the results with previous experimental studies by Hatcher *et al.* (2000); Tanino *et al.* (2005); Testik & Yilmaz (2015). Testik & Ungarish (2016) solved a more general model, in which the drag force is proportional to $|u|^\lambda$, with u being the horizontal velocity and λ a constant positive value. They found four classes of similarity solutions: Class I describes GCs with a triangular shape and constant velocity at the nose, which is developed with a continuous-release source; Class II GCs have a

fixed height at the source and a nonlinear profile, but with no experimental evidence yet; Class III corresponds to constant-volume GCs with a linearly increasing velocity toward the nose; all other continuous-release GCs belong to Class IV.

The present experimental activity refers to GCs in a cylindrical axisymmetric geometry in the presence of artificial vegetation, to achieve more insights of the physical process. This configuration is representative of many environmental scenarios (see Chowdhury & Testik 2014, for a long list), for example in the presence of localized inputs in the absence of flow channelization, or during disposal operations of dredged materials for beaches and wetland restoration (pipelines for conveying mixtures of water and sediment have a terminal that represents a localised source, coinciding with the origin of a radially symmetrical discharge, and trigger turbidity currents; pile and sheet pile driving in a lake or marine environments generates radially symmetrical turbidity currents, which pose an environmental risk and disturbance to aquatic species). These GCs in radial geometry appear of particular interest, compared to the case of GCs confined in rectangular (non-divergent) geometry.

We conducted 40 experiments with two different density of the array of the artificial vegetation: 12 in lock-release configuration, 13 in constant inflow rate, 9 in waxing and 6 in waning inflow rate. To the best of our knowledge, the experiments are original and new, and no similar experiments are available in literature.

Although the vegetation of our experiments is artificial, with pragmatical choices of the dimensions of the rods dictated by experimental needs and by commercial availability of the stuff requested for the set-up, the adopted pattern reflects realistic aquatic vegetation. In fact, defining the frontal area per unit volume $a = D/s^2$, where s is the spacing between rods, our experimental configuration corresponds to $a = 0.066 - 0.138 \text{ cm}^{-1}$, which is equivalent to Marsh grasses with $a = 0.01 - 0.07 \text{ cm}^{-1}$, Seagrasses with $a = 0.01 - 0.07 \text{ cm}^{-1}$ and Mangroves, with a up to 0.2 cm^{-1} (Nepf 2012).

The available theoretical models point out that GC propagation analysis is inconclusive when the value of λ is not known (Testik & Ungarish 2016), hence we measured the drag exponent, with the same pattern of rods adopted for GCs experiments (same density) and for different values of the Reynolds number. We also expect the λ exponent of drag to be a function not only of Reynolds number and density of the obstacles, but also of other geometric characteristics of the obstacles, such as, for example, the frontal area per unit volume (see, e.g. Ozan *et al.* 2015) or the diameter of the rods or of an equivalent size for other obstacles. If the flow of the GCs were in a classical porous medium, we would expect a dependence on “permeability”; in the present case we expect a dependence on the spacing between obstacles or on the diameter of the rods, and two further drag measurements were performed with a different diameter of the rods in order to elucidate this aspect. However, we bear in mind that the goal of the present analysis is not the identification of such a dependence, but more pragmatically the estimation of the exponent λ to be used for the interpretation of the experiments. The physical limits are $\lambda = 1$ for viscous drag at low Reynolds number, and $\lambda = 2$ in fully turbulent regime at high Reynolds number.

The paper is organized as follows. Section 2 briefly introduces the theoretical model, section 3 describes the experimental layout and procedures, section 4 provides details and discussion on the experiments. The conclusions are drawn in section 5. The results of drag measurements with different rods diameters are analysed in the Appendix A, where scaling of drag is discussed with respect to the density and the diameter of the rods.

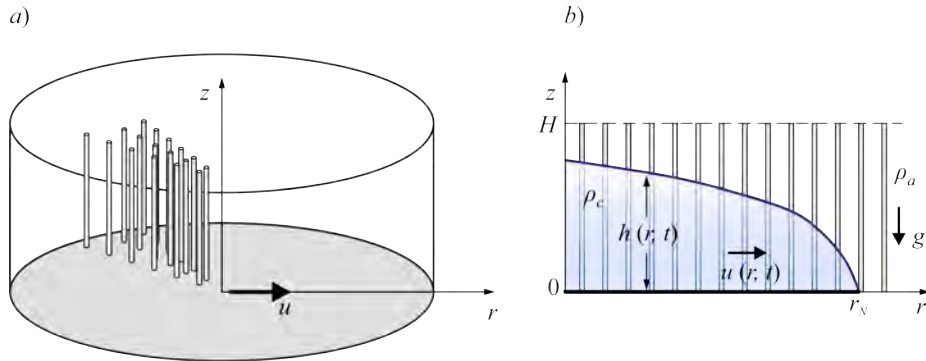


FIGURE 1. Sketch of the theoretical model: a) 3D schematic; b) axial-radial plane section.

2. Theoretical model for vegetation domain

2.1. Formulation

Here we present the essentials of the theoretical model used in our investigation. This model served a guideline for the design and setup of the experiments, and it is also used for comparisons with, and interpretation of, the data and effects recorded in our experiments. We note that the model has been presented before (Hatcher *et al.* 2000; Testik & Ungarish 2016). The novelty here is the application of new influx conditions and the comparison with experiments aiming to an estimate of the power-law λ and to measure the front position and the profile of the currents.

We use a cylindrical coordinate system, and assume axial symmetry (i.e., zero or negligibly-small dependency on the angular coordinate). We consider rod-like vegetation which fills a horizontal domain of height H . In our system of reference, the coordinate r is horizontal, while z is vertical upward. The GC propagates in the r direction, see figure 1a. The densities of the current and ambient fluids are ρ_c and ρ_a , with $\rho_a < \rho_c$, and $z = 0$ and $z = H$ are rigid boundaries, see figure 1b. For practical reasons, $z = H$ in the experiments is a free surface, see next discussions on the sensitivity of the results to this approximation). The height (thickness) of the current is $h(r, t)$, and the height-averaged speed of the current is $u(r, t)$, while that of the ambient is $u_a(r, t)$. The radius of propagation is $r_N(t)$.

The equations of motion are derived along the lines of the thin-layer simplification detailed in Ungarish (2020). We use dimensional variables unless stated otherwise.

2.2. Equations of motion and boundary conditions

We start with the observation that the thickness of the ambient-fluid layer is $H - h$ and by continuity

$$u_a = -uh/(H - h). \quad (2.1)$$

for constant H . The vegetation introduces a drag force. As suggested by previous investigations and confirmed by our experiments, the effective drag per unit volume of fluid is proportional to the density of the fluid and to the speed at some power $\lambda \geq 1$. To facilitate the analysis, we assume that (i) the coefficient of proportionality is a constant, \tilde{c} ; (ii) in a given GC system, both the current and the ambient have the same \tilde{c} and λ (as it will be evident in the following steps, the accuracy of this assumption is not relevant since we will adopt a single-layer model where only the dynamics of the dense current is considered). We assume (and confirmed by order of magnitude estimates of the laboratory data) that in the tests considered here, the viscous and turbulent stresses in the

current and ambient domains are negligible as compared to the other forces. We consider flow fields in which the drag dominates the acceleration (inertia) term. Therefore, in the subsequent analysis the Du/Dt terms are neglected, except for the analysis of transition, see eq.(2.7). The pressure is approximated by the hydrostatic balance, and hence the x -momentum balances for the ambient and current reduce to

$$0 = -\frac{\partial p}{\partial x} - \rho_a \tilde{c} u_a |u_a|^{\lambda-1}, \quad 0 = -\frac{\partial p}{\partial x} - (\rho_c - \rho_a) g \frac{\partial h}{\partial r} - \rho_c \tilde{c} u |u|^{\lambda-1}, \quad (2.2)$$

where p is the pressure in the ambient and g the gravity acceleration. λ is assumed to be constant. Elimination of the pressure and use of (2.1) yield one combined-momentum equation for u . Consequently, the motion can be expressed as the system of continuity and momentum balances

$$\sigma \frac{\partial h}{\partial t} + \frac{\partial hu}{\partial r} = -\frac{uh}{r}; \quad (2.3)$$

$$-g' \frac{\partial h}{\partial r} - \tilde{c} |u|^{\lambda-1} u \left[1 + \frac{\rho_a}{\rho_c} \left(\frac{h}{H-h} \right)^\lambda \right] = 0, \quad (2.4)$$

where the reduced gravity is $g' = g(1 - \rho_a/\rho_c)$, and σ is the porosity of the vegetation medium in which the fluids move, always positive and smaller than 1, assumed here constant. We also define the density of the vegetation as $\kappa = 1 - \sigma$.

Further simplifications of the equations are possible and useful. First, we introduce the coordinate-stretching of the time to t/σ ; this eliminates σ from the subsequent analysis. Second, we note that the Boussinesq system with $\rho_c \approx \rho_a$ admits the simplification of the drag term in the momentum equation (2.4) by setting $\rho_a/\rho_c = 1$ in front of the term $h/(H-h)$ which expresses the drag coupling between the current and the upper ambient fluid. Next, for a deep current $h/H \ll 1$, the coupling term can be neglected. This simplification, also called the one-layer model, is facilitated by the fact that the value of λ is larger than 1 and typically 2. In the range of parameters considered in the present investigation, the model based on Boussinesq and one-layer simplifications is expected to provide a fair approximation to the main behaviour (propagation and shape) of the current. The one-layer theory is an approximation that is expected to work well when the height of the current to ambient at $r/r_N \approx 0.5$ is less than 0.5 (which implies that a significant part of the current is even thinner), and when the rate of increase of the height due to influx is much smaller than the speed of propagation. (We keep in mind that h decreases with r and that the propagation of the current is governed by the ring of fluid close to r_N). Consequently, we shall use the momentum equation

$$0 = -g' \frac{\partial h}{\partial r} - \tilde{c} |u|^{\lambda-1} u, \quad (2.5)$$

which expresses the balance between the buoyancy driving force and the vegetation-drag hindering effects on the layer of the dense fluid. We note that the curvature terms are not present in this balance; however, the curvature effect is strongly manifested in the r.h.s. continuity eq.(2.3) and hence the present geometry needs a separate investigation from the 2D counterpart.

We emphasize that the coefficient \tilde{c} in the drag term is different from the classical dimensionless ‘‘drag coefficient’’ defined by the ratio of non-viscous opposing force on a body to dynamic pressure. The present drag coefficient is defined by the ratio of the opposing force between vegetation and fluid, per unit volume of fluid, divided by $\rho|u|^\lambda$ (the density and speed pertain to either the domain of the current or ambient), and \tilde{c} is dimensional with $[\tilde{c}] = L^{1-\lambda} T^{\lambda-2}$.

In general, the volume of the current is known. This can be expressed as

$$\int_0^{r_N(t)} r h(r, t) dr = qt^\alpha \equiv \mathcal{V}(t), \quad (2.6)$$

where q and $\alpha \geq 0$ are given. Note that $\mathcal{V}(t)$ is the volume per radian, and contains both fluid and vegetation.

At the nose $r = r_N(t)$, we impose the condition $h = 0$ while u_N is finite. The justification is as follows. The motion takes place because the buoyancy driving $g'(-\partial h/\partial r)$ in the radial direction balances the opposing drag $\sim -|u|^{\lambda-1}u$. This means that, at any radial position of the moving current, a negative slope $\partial h/\partial r$ is present, and hence h is expected to decrease to 0 at the nose. The subsidiary assumption is that a nose of zero thickness (i.e., a contact line) is compatible with the equations of motion, and this will be confirmed later. (We note in passing that a moving contact-line condition is an abstraction of a complex r -thin corner region in which strong gradients are present, and hence in practice the decrease to $h = 0$ is less sharp than in the theory. There is evidence from the viscous-current counterpart, see Ungarish (2020), that this singularity has little effect on the speed of propagation, because the larger h creates a larger buoyancy drive from the dense material behind. We conjecture that the same behaviour occurs in the present case.) In this context we also note that it is possible to eliminate u from (2.3) and (2.5) to obtain one equation for $h(r, t)$, which bears similarity with the formulation for power-law fluids GCs, see for example Sayag & Worster (2013).

For the boundary conditions at the axis $r = 0$, we must distinguish between the following cases: (i) fixed volume (or lock-release) admits the simple $u = 0$ at $r = 0$; (ii) for GCs created by influx, it is in general difficult to prescribe the precise boundary condition at the source. What we usually know is the total volume flux. Near the axis, the influx speed may be large and the thin-layer assumptions may be invalid. From the point of view of the present set of equations, this domain is a singularity. For progress, we apply the usual assumption that there is some adjustment domain in which the flux is matched with the values of h imposed by the outer region. The relative volume of fluid in this singular region is expected to be small with respect to the volume of the dense fluid, (the radial geometry embeds a bottom area growth proportional to the square of the radius, and we are considering the region near the axis) and, hence, of little relevance to the major flow field (see Di Federico *et al.* 2012). The generally-accepted mathematical solution for the axisymmetric current created by influx imposes the conditions at the nose, but leaves open the behaviour near the axis. We shall keep this in mind during the comparisons with realistic data.

In the present simplified model, we cannot apply realistic initial conditions of u and h at $t = 0$. The physical meaning is that the initial inertial adjustment is missed, and we assume that this adjustment is a short episode, whose details are insignificant to the subsequent motion.

2.3. Regimes of gravity currents

An estimate of the transition from buoyancy-inertial to buoyancy-drag (turbulent drag) regime can be obtained by imposing that the flow inertia, drag and buoyancy terms are of the same order of magnitude:

$$\frac{\partial u}{\partial t} \sim g' \frac{\partial h}{\partial r} \sim \tilde{c}|u|^{\lambda-1}u, \quad (2.7)$$

while the mass conservation in integral form brings to $hr^2 \sim \mathcal{V}$. By assuming that $r \sim ut_c$ and $\mathcal{V} = qt^\alpha$, and defining t_c as the time of transition, it results

$$\frac{u}{t_c} \sim g' \frac{h}{ut_c} \sim \tilde{c}u^\lambda, \quad hu^2t_c^2 \sim qt_c^\alpha, \quad (2.8)$$

which leads to the scaling

$$t_c \sim \left(g' q \tilde{c}^{4/(\lambda-1)} \right)^{(1-\lambda)/[\alpha(\lambda-1)-2\lambda+6]}, \quad (2.9)$$

equal to

$$t_c \sim \tilde{c}^{-1}; \left(\tilde{c}^4 g' q \right)^{-1/(\alpha+2)} \quad \text{for } \lambda = 1, 2. \quad (2.10)$$

The critical time increases with λ and decreases with α . Later on a viscous-buoyancy balance dominates, at a time obtained by imposing that the viscous drag, turbulent drag and buoyancy terms are of the same order of magnitude:

$$\nu \frac{\partial^2 u}{\partial y^2} \sim g' \frac{\partial h}{\partial r} \sim \tilde{c}|u|^{\lambda-1}u, \quad (2.11)$$

or

$$\frac{12\nu u}{h^2} \sim g' \frac{h}{ut_{v1}} \sim \tilde{c}u^\lambda, \quad hu^2t_{v1}^2 \sim qt_{v1}^\alpha, \quad (2.12)$$

which leads to the scaling

$$t_{v1} \sim \left(\frac{g'q}{\tilde{c}} \right)^{1/(3-\alpha)} \left(\frac{\tilde{c}h^2}{12\nu} \right)^{(3+\lambda)/[(\lambda-1)(3-\alpha)]}. \quad (2.13)$$

By considering the viscous drag due to the obstacles instead of the viscous drag due to the bottom, results in

$$\frac{\kappa\nu u}{s^2} \sim g' \frac{h}{ut_{v2}} \sim \tilde{c}u^\lambda, \quad hu^2t_{v2}^2 \sim qt_{v2}^\alpha, \quad (2.14)$$

where s is a scale of the spacing of the obstacles and κ is the density of the obstacles. The corresponding time of transition is

$$t_{v2} \sim \left(\frac{g'q}{\tilde{c}} \right)^{1/(3-\alpha)} \left(\frac{\tilde{c}s^2}{\kappa\nu} \right)^{(3+\lambda)/[(\lambda-1)(3-\alpha)]}. \quad (2.15)$$

Note that for $\lambda = 1$ the two times t_{v1} and t_{v2} are undefined since viscous resistance and drag scale with u and are indistinguishable. In conclusion, the obtained self-similar solution is intermediate asymptotic in the interval $t_c < t < t_v$ where $t_v = \min(t_{v1}, t_{v2})$. The condition $t_{v2} < t_{v1}$ corresponding to viscous drag due to vegetation dominating with respect to the viscous drag due to the bottom, for $\alpha < 3$ requires that $s < h\sqrt{\kappa/12}$, which for $\kappa = 0.10$ and $h = 1$ cm indicates $s \approx 1$ mm, a condition generally not satisfied. A waxing inflow rate with $\alpha > 3$ is unrealistic and, moreover, we expect it to occur for a short time interval, not sufficient to allow viscosity to dominate the balance with buoyancy. For this reason, we limit our analysis to a viscous-buoyancy balance regime due to the floor of the tank and not to the vegetation. The previous results for $\lambda = 2$ correspond to values given in Hatcher *et al.* (2000).

Eq.(2.13) can be also expressed as a function of the parameters of the flow process as

$$t_{v1} \sim \left(\frac{g'q}{\tilde{c}} \right)^{(3\lambda+1)/[7\lambda-3-\alpha(3\lambda+1)]} \left(\frac{\tilde{c}^3}{12\nu g'^2} \right)^{(\lambda+3)/[7\lambda-3-\alpha(3\lambda+1)]}, \quad (2.16)$$

where h , retained in eq.(2.13) only for comparing t_{v1} and t_{v2} , has been eliminated. Equating eq.(2.9) and eq.(2.16) yields a timescale t^* and volume coefficient scale q^*

$$t^* = \left[\frac{1}{(12\nu g'^2)^{(\lambda-1)} \tilde{c}^4} \right]^{1/(\lambda+3)}, \quad (2.17)$$

$$q^* = \left[\frac{(12\nu g'^2)^{\alpha(\lambda-1)-2\lambda+6}}{g' \tilde{c}^{4(3-\alpha)}} \right]^{1/(\lambda+3)}, \quad (2.18)$$

that allow us to express the two times in dimensionless form:

$$\tilde{t}_c \sim \tilde{q}^{(1-\lambda)/[\alpha(\lambda-1)-2\lambda+6]}, \quad (2.19)$$

and

$$\tilde{t}_{v1} \sim \tilde{q}^{(3\lambda+1)/[7\lambda-3-\alpha(3\lambda+1)]}, \quad (2.20)$$

where $\tilde{t} = t/t^*$ and $\tilde{q} = q/q^*$. The exponent in eq.(2.19) is always negative for $1 < \lambda < 2$ and $\alpha > 0$, and \tilde{t}_c monotonically decreases with \tilde{q} . The exponent in eq.(2.20) is positive if $\alpha < \alpha_c \equiv (7\lambda - 3)/(3\lambda + 1)$ and it is negative otherwise. Figure 2a shows the theoretical dimensionless times versus the volume coefficient, as a function of α and for $\alpha < \alpha_c$. The hatched area refers to $\alpha = 0$ and $\lambda = 2$ and is the domain of existence of an intermediate asymptotic similarity solution, which is possible only for $\tilde{q} > 1$: the initial stage of the GC is dominated by inertia, which progressively becomes less important leaving space to turbulent drag of the vegetation. The turbulent drag-buoyancy balance is finally substituted by a viscous-buoyancy balance. The domain of existence of the turbulent drag-buoyancy balance widens with α and also for reduced λ , and for $\alpha \rightarrow \alpha_c$ viscosity never dominates over turbulent drag.

Figure 2b shows the same data of figure 2a for $\alpha > \alpha_c$, with the hatched area referring to $\alpha = 2$ and $\lambda = 2$. The intermediate asymptotic similarity solution is allowed only for $\tilde{q} < 1$, the domain of existence becomes smaller for increasing $\alpha > \alpha_c$.

This analysis is approximate because it refers to homogeneous and invariant assumptions for h , u and for λ , \tilde{c} , which in real GCs are variable in space and time. In particular, near the front the current is always in the viscous-buoyancy balance regime. However, it provides useful insights to discuss the deviations of the theoretical model from experiments and to frame the validity limits of a self-similar solution.

2.4. Solution

When \tilde{c} and λ are constant and the volume is of the form $\mathcal{V} = qt^\alpha$ (including the fixed-volume lock-release case $\alpha = 0$) analytical solutions of similarity type can be obtained, as follows.

Let $y = r/r_N(t)$. The equations of motion can be expressed in terms of the variables $h(y, t)$ and $u(y, t)$. The domain of solution is $y \in [0, 1]$ and the nose of the current is at $y = 1$. We seek a similarity solution of the form

$$r_N = \mathcal{K}t^\gamma, \quad h = t^\delta \mathcal{H}(y), \quad u = \dot{r}_N \mathcal{U}(y), \quad (2.21)$$

where the upper dot denotes time derivative and $\mathcal{K}, \gamma, \delta$ are constants. The task is to obtain the values of $\mathcal{K}, \gamma, \delta$ and the profiles $\tilde{\mathcal{H}}(y), \mathcal{U}(y)$ subject to the boundary conditions. The boundary conditions at the nose ($y = 1$) are $\mathcal{U}(1) = 1, \mathcal{H}(1) = 0$. The global volume balance (per radian) is

$$\mathcal{V} = \int_0^{r_N} hr \, dr = \mathcal{K}^2 t^{2\gamma} t^\delta \int_0^1 \mathcal{H}(y)y \, dy = qt^\alpha; \quad (2.22)$$

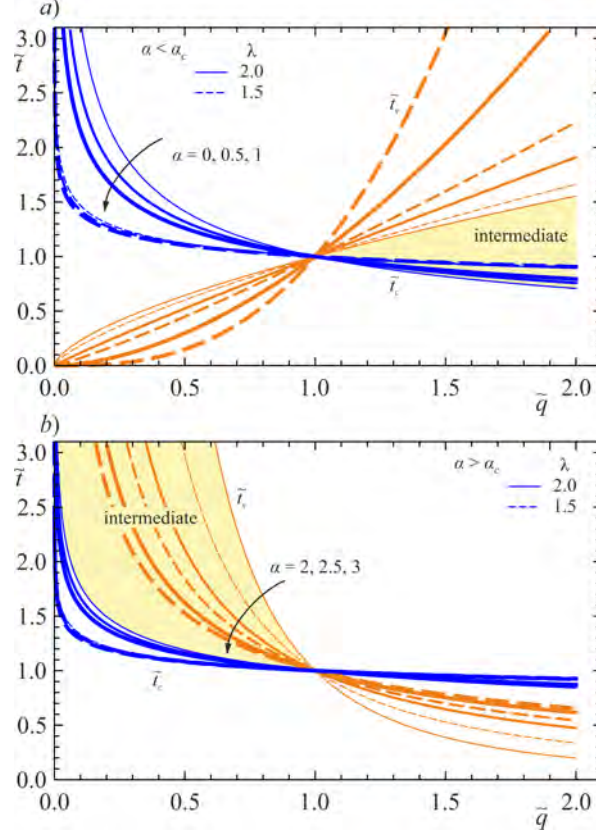


FIGURE 2. Evolution of the balance regime for a radial GC in the presence of vegetation as a function of the time exponent of the volume of denser fluid. *a*) Diagrams for $\alpha < \alpha_c \equiv (7\lambda - 3)/(3\lambda + 1)$ and *b*) for $\alpha > \alpha_c$. The continuous curves refer to $\lambda = 2$, the dashed curves refer to $\lambda = 1.5$. The hatched areas represent the domain where the intermediate asymptotic solution exists with turbulent drag-buoyancy balance; the intermediate asymptotic solution regime occurs after the initial phase, dominated by inertia, ending before the phase when viscosity is dominant.

and yields

$$2\gamma + \delta = \alpha; \quad \mathcal{K}^2 J = q, \quad (2.23)$$

where $J = \int_0^1 \mathcal{H}(y)y dy$.

Substitution of the similarity form (2.21) into the momentum equation (2.5) yields, after some algebra

$$\delta = -\lambda + \gamma(\lambda + 1); \quad (2.24)$$

$$|\mathcal{U}(y)|^{\lambda-1} \mathcal{U}(y) = -\tilde{\mathcal{H}}'(y) \quad (2.25)$$

where

$$\tilde{\mathcal{H}}(y) = \frac{\mathcal{H}(y)}{C}; \quad C = \frac{\tilde{c}}{g'} \gamma^\lambda \mathcal{K}^{1+\lambda}. \quad (2.26)$$

Combining (2.23) with (2.24) we find

$$\gamma = \frac{\alpha + \lambda}{3 + \lambda}. \quad (2.27)$$

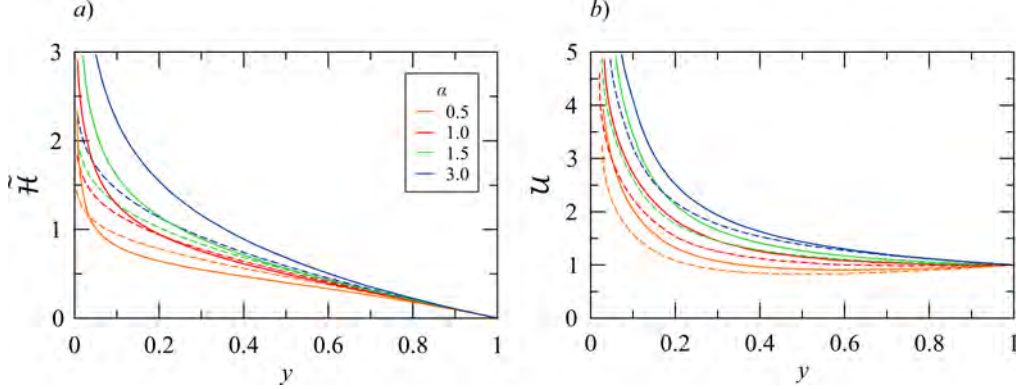


FIGURE 3. Theoretical profiles (a) $\tilde{\mathcal{H}}$ and (b) \mathcal{U} as functions of y for $\alpha = 0.5 - 3$, $\lambda = 1$ (dotted lines) and $\lambda = 2$ (solid lines).

The continuity equation reads

$$\frac{\delta}{\gamma} \tilde{\mathcal{H}}(y) + (\mathcal{U} - y) \tilde{\mathcal{H}}'(y) + \tilde{\mathcal{H}}(y) \mathcal{U}'(y) = -\frac{\mathcal{U}}{y} \tilde{\mathcal{H}}(y). \quad (2.28)$$

For given λ and α we obtain γ and δ by equations (2.27) and (2.24), then solve equations (2.25) and (2.28). Note that $\mathcal{U}(y)$ and $\tilde{\mathcal{H}}(y)$ are dimensionless. An analytical solution of equations (2.25) and (2.28) can be obtained for $\delta/\gamma = -2$:

$$\mathcal{U} = y; \quad \tilde{\mathcal{H}}(y) = \frac{1}{1 + \lambda} (1 - y^{1+\lambda}). \quad (2.29)$$

This is valid when

$$\gamma = \frac{\lambda}{3 + \lambda}; \quad \delta = -2\gamma; \quad \alpha = 0. \quad (2.30)$$

The validity of this result can be verified by direct substitution into the equations of motion, and it is evident that the boundary conditions $\mathcal{U}(0) = 0$, $\tilde{\mathcal{H}}(1) = 0$ are satisfied. This describes the propagation of a GC of fixed volume.

For influx values of $\alpha > 0$ the similarity profiles can be calculated by numerical integration. Typical results are shown in figure 3. We recall that the solution is irrelevant for small y , because a realistic source must have a finite radius. On the other hand, the solution is well-behaved about the nose. Using an expansion in powers of $1 - y$, we find that for small values of $1 - y$ the solution of (2.25) and (2.28) can be approximated by

$$\tilde{\mathcal{H}} = (1 - y) + \lambda \frac{\delta}{4\gamma} (1 - y)^2 + \dots, \quad \mathcal{U} = 1 + \frac{\delta}{2\gamma} (1 - y) + \dots \quad (2.31)$$

Consequently, for given α and λ we calculate the profiles $\mathcal{U}(y)$, $\tilde{\mathcal{H}}(y)$ by numerical integration from $y = 1 - \Delta$ to smaller values of y . Here Δ is some small interval which allows the application of the approximation (2.31) as the initial condition for the integration, thus avoiding the problem of the zero coefficient of $\mathcal{U}'(1)$ in (2.28).

For $\alpha = 3$ we find $\gamma = \delta = 1$ independent of λ ; the aspect ratio of the current does not change with t . Typical solutions with influx conditions relevant to the present investigation are illustrated in figure 3.

The front position in dimensional variables is

$$r_N = \left(\frac{qg'}{\tilde{c}\gamma^\lambda \tilde{J}} \right)^{1/(3+\lambda)} t^\gamma, \quad (2.32)$$

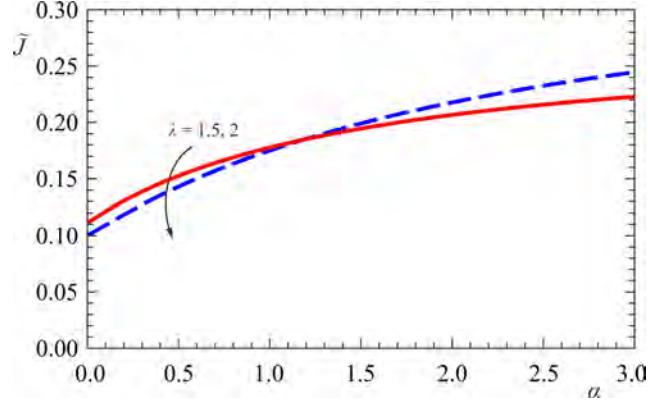


FIGURE 4. Value of the integral \tilde{J} as a function of α for $\lambda = 1.5, 2$.

where $\tilde{J} = \int_0^1 \tilde{\mathcal{H}}(y) y dy$, which for $\alpha = 0$ becomes

$$r_N = \left(\frac{qg'}{\tilde{c}} \right)^{1/(3+\lambda)} \left[\frac{2(3+\lambda)^{\lambda+1}}{\lambda^\lambda} \right]^{1/(3+\lambda)} t^{1/(3+\lambda)}. \quad (2.33)$$

Figure 4 shows the numerical value of \tilde{J} for different α and λ .

3. The experimental layout and procedures

3.1. Set-up for the gravity currents

We ran a series of experiments at the Hydraulic Laboratory of the University of Parma. Our tank was a poly-methyl-methacrylate circular sector, with a radius of $R = 180$ cm and an angle $\beta = 30^\circ$ as sketched in figure 5a. The vegetation was modelled by (i) a number of 200 vertical plastic rods, with a density $\kappa = 0.050$, as sketched in figure 5a, and (ii) a number of 320 rods, with a density $\kappa = 0.081$. The rods, with diameter $D = 1.6$ cm, were positioned according to an equilateral triangular mesh grid, with the edge of the triangles equal to 5.6 cm for $\kappa = 0.050$ and 5.0 cm for $\kappa = 0.081$.

For the lock-release experiments, a stainless steel gate 0.2 cm thick was positioned at $r_0 = 55$ cm and manually lifted just before the start of the experiment, see figure 5b. The opening of the gate took approximately 0.2 s, a negligible time when compared to the duration of the experiments, $t = 40 - 60$ s. A criterion for establishing the maximum gate opening time was formulated by Lauber & Hager (1998) for dam breaks on a dry horizontal bottom with a vertical lift gate: if the opening occurs in a time greater than $t_{min} = \sqrt{2h_0/g'}$, the initial flow field is distorted by the presence of the flat gate surface, increasing the discrepancy between theory and experiments. Applying this criterion, the critical condition for this experimental activity corresponds to $t_{min} = 0.8$ s, more than the opening time of 0.2 s for the present experiments.

For the experiments with a continuous source of flux, a home-made diffuser was inserted at $r_0 = 25$ cm, see figure 5c. The diffuser was connected to a pump controlled in feedback by a LabView software. Different experiments were conducted with a constant, waxing or waning volume inflow rate.

The lateral view of the experiments was recorded by a full HD video-camera (1920 pixels \times 1080 pixels, iPhone 7, Apple Inc.), working at 30 frames per second (fps). A 5 cm square grid stuck on the inner side of the front lateral wall was used for converting pixels into laboratory coordinates, with the aid of a proprietary Matlab code. The algorithm

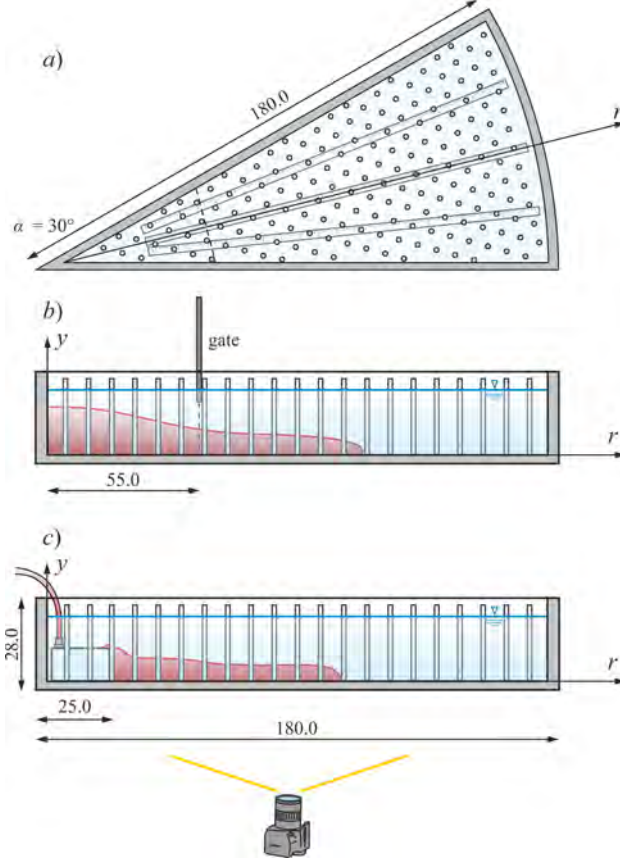


FIGURE 5. Experimental set-up with $\kappa = 0.050$. *a)* Top view; *b)* lateral view of a lock-release experiment and *c)* lateral view of a continuous flux experiment. Units are in centimetres. Images are not corrected for distortion.

preliminary requires i) the acquisition of the pixels of the knots of the grid; ii) the computation of a conversion polynomial function for the two horizontal and vertical directions, mapping pixels into laboratory coordinates. The order of the polynomial is automatically chosen to minimize the root-mean-square deviation between the grid knots in laboratory coordinates and the reconstructed values starting from the pixels in the image. The conversion polynomials allow compensating for defects in the optics and for the position of the camera (Longo *et al.* 2015, 2016), and are used to transform the pixels corresponding to the instantaneous profile of the current into laboratory coordinates.

The top view was recorded by a 4k video-camera (3840 pixels \times 2160 pixels, iPhone 11, Apple Inc.), working at 30 fps. The time evolution of the position of the nose of the current was measured by means of three radial grids glued at the base of the tank. High-frequency neon lamps provided stable and homogeneous illumination at the back wall of the tank.

Softened tap water, with density $\rho_a = 1000 \text{ kg m}^{-3}$, was always used as ambient fluid, although sometimes $\rho_a = 1001 - 1002 \text{ kg m}^{-3}$ because of salty traces left from previous experiments. The dense current was made of tap water, sodium chloride (NaCl) and red aniline dye, well mixed before the use.

For numerous practical reasons, the fixed top condition is replaced by the free-surface condition, with no lid on the top of the tank. There is theoretical and experimental

evidence that for Boussinesq systems (as considered in this paper) the difference between fixed and open-top has negligible influence on the flow of the current, see Ungarish (2020).

In order to have an estimate of the mixing between the current and the ambient, some samples of the dense fluid were collected during some experiments listed in table 1, at the bottom of the current and a few millimetres below the interface, at $r = 90, 170, 175$ cm. The samples were manually collected with a syringe connected to a 2 mm brass pipe, and then analysed with a refractometer.

Appendix A describes further experiments for measuring the drag coefficient of a set of rods, in the same configuration adopted for the GCs experiments.

3.2. The uncertainty in variables and parameters

We considered the instrument accuracy and the sequence of operations during tests to estimate the uncertainty of the variables and parameters. Hydrometers with an accuracy of 10^{-3} g cm $^{-3}$ were used to measure density, hence the corresponding uncertainty for the reduced gravity $g' = (1 - \rho_a/\rho_c)g$ is $\Delta g'/g' \leq 0.2\%$. The level of the dense fluid in the lock and the level of the ambient fluid were measured by a ruler with an accuracy of 0.2 cm. The relative uncertainty is $\Delta h_0/h_0 \leq 2\%$. The volumetric flow rate of the pump was controlled within 1% of accuracy.

The Reynolds number of the current has an uncertainty $\Delta Re/Re \leq 4\%$, also based on the assumption of an uncertainty of 1% in estimating the kinematic viscosity of salty water. The resolution in grabbing the lateral profiles of the dense current is approximately 0.1 cm pixel $^{-1}$, while the overall uncertainty due to parallax errors is approximately 0.3 cm.

The velocity of water during drag coefficient measurements has an uncertainty $\Delta V/V = 2\%$ at high inflow rates and $\Delta V/V = 4\%$ at low inflow rates. Reynolds number of the vegetation has an uncertainty $\Delta Re_{rod}/Re_{rod} \leq 6\%$ and the arrangement for measuring the drag force gives results with an uncertainty less than 10%.

The inflow produces an increase of the level of the ambient fluid. The underlying idea of the thin-layer model is that the vertical velocity is much smaller than the horizontal velocity, $w \ll u$. If we consider a constant inflow rate q , the rate of increase of level can be expressed as $w = 2q/(\beta R^2)$, $\beta = 30^\circ$, which for the largest value $q = 400$ cm 3 s $^{-1}$ of our experiments (exp. 33 in table 1) results in $w = 0.04$ cm s $^{-1}$, compared to a typical radial speed of $u = 10$ cm s $^{-1}$, hence the condition $w \ll u$ is satisfied. Over 25 s of experiment, the variation of the ambient fluid level equals $\Delta H = 1$ cm, representing 5.2% of the initial ambient fluid $H = 19$ cm. This value is reached at the end of the experiment, and on the average, $\Delta H/H = 2.6\%$ which is in the range of the other experimental errors. In most of the other experiments the $\Delta H/H$ is much smaller because q is smaller and even null for lock-release experiments.

4. The experiments

Table 1 lists the parameters of the experiments. Experiments 1–4 were in a lock-release (LR) configuration and with no vegetation $\kappa = 0$, in order to check the overall quality of the set-up in a simple configuration, without the effects of the rods. Experiments 5–29 were with a vegetation density of $\kappa = 0.050$, experiments 5–10 were LR while experiments 11–29 involved a continuous source of flux, constant or time varying. Finally, experiments 30–40 were with a vegetation density of $\kappa = 0.081$ and a constant source of flux.

Figure 6 shows some snapshots of the lateral view of the tank taken at $t = 0-4-8-16$

Exp.	ρ_a (kg m^{-3})	ρ_c (kg m^{-3})	g' (cm s^{-2})	H (cm)	h_0 (cm)	q' ($\text{cm}^3 \text{s}^{-\alpha}$)	α	κ	γ_{th} ($\lambda = 1$)	γ_{th} ($\lambda = 2$)	γ_{exp}	U (cm s^{-1})	T (s)	remark
1	1000	1030	29.4	20.0	20.0	15 100	0	0	0.50	0.50	0.55 ± 0.01	24.3	0.82	LR (f)
2	1000	1017	16.7	20.0	20.0	15 100	0		0.50	0.50	0.55	18.3	1.10	(f)
3	1001	1018	16.7	20.0	10.0	7550	0		0.50	0.50	0.50	18.3	1.10	(p)
4	1000	1017	16.7	20.0	15.0	11 300	0		0.50	0.50	0.50	18.3	1.10	(p)
5	1000	1032	31.4	20.0	20.0	15 100	0	0.050	0.25	0.40	0.46	25.1	0.80	LR (f)
6	1000	1017	16.7	19.4	9.7	7300	0		0.25	0.40	0.41	18.0	1.08	(p)
7	1002	1017	14.7	19.4	15.0	11 300	0		0.25	0.40	0.39	16.9	1.15	(p)
8	1000	1017	16.7	19.3	19.3	14 550	0		0.25	0.40	0.48	17.9	1.08	(f)
9	1002	1030	27.4	19.9	10.1	7600	0		0.25	0.40	0.43	23.4	0.85	(p)
10	1002	1030	27.4	19.2	15.0	11 300	0		0.25	0.40	0.45	22.9	0.84	(p)
11	1000	1021	20.6	19.0	-	200	1		0.50	0.60	0.57	19.8	0.96	CF
12	1000	1021	20.6	19.4	-	100	1		0.50	0.60	0.61	20.0	0.97	
13	1000	1035	34.3	19.0	-	100	1		0.50	0.60	0.58	25.5	0.74	
14	1000	1057	55.9	19.0	-	100	1		0.50	0.60	0.63	32.6	0.58	
15	1001	1055	52.9	19.0	-	200	1		0.50	0.60	0.60	31.7	0.60	
16	1000	1055	53.9	19.0	-	50	1		0.50	0.60	0.48	32.0	0.59	
17	1000	1055	53.9	19.0	-	150	1		0.50	0.60	0.54	32.0	0.59	
18	1000	1037	36.3	19.0	-	200	1		0.50	0.60	0.54	26.3	0.72	
19	1000	1035	34.3	19.0	-	50	1		0.50	0.60	0.67 ± 0.02	25.5	0.74	
20	1000	1038	37.3	19.0	-	0.264	2.50		0.88	0.90	0.87 ± 0.03	26.6	0.71	WX
21	1000	1020	19.6	20.0	-	0.264	2.50		0.88	0.90	0.85 ± 0.01	19.8	1.01	
22	1000	1020	19.6	19.0	-	0.037	3.00		1.00	1.00	0.99	19.3	0.98	
23	1000	1036	35.3	19.0	-	0.037	3.00		1.00	1.00	0.91	25.9	0.73	
24	1000	1023	22.6	19.0	-	16.17	1.67		0.67	0.73	0.74	20.7	0.92	
25	1000	1043	42.2	19.0	-	15.48	1.68		0.67	0.74	0.74	28.3	0.67	
26	1000	1021	20.6	19.0	-	580	0.76		0.44	0.55	0.59	19.8	0.96	WN
27	1000	1020	19.6	19.0	-	2153	0.45		0.36	0.49	0.60	19.3	0.98	
28	1001	1038	36.2	19.0	-	2074	0.46		0.37	0.49	0.63	26.2	0.72	
29	1001	1037	35.3	19.0	-	547	0.78		0.45	0.56	0.64	25.9	0.73	
30	1000	1102	100.0	19.0	-	300	1	0.081	0.50	0.60	0.57	43.6	0.44	CF
31	1000	1186	182.4	19.0	-	300	1		0.50	0.60	0.57	58.9	0.32	
32	1000	1020	19.6	19.0	-	170	1		0.50	0.60	0.55	19.3	0.98	
33	1000	1100	98.1	19.0	-	400	1		0.50	0.60	0.58	43.2	0.44	
34	1000	1100	98.1	19.0	-	11.92	1.72		0.74	0.74	0.69	43.2	0.44	WX
35	1000	1100	98.1	20.0	-	3.48	2.70		0.94	0.94	0.99 ± 0.04	44.3	0.45	
36	1000	1100	98.1	19.0	-	0.24	2.50		0.90	0.90	0.81 ± 0.04	43.2	0.44	
37	1000	1100	98.1	19.0	-	597	0.77		0.55	0.55	0.55 ± 0.01	43.2	0.44	WN
38	1000	1100	98.1	19.0	-	2436	0.39		0.48	0.48	0.53	43.2	0.44	
38	1000	1100	98.1	19.5	19.5	14 700	0		0.40	0.40	0.43	43.7	0.45	LR (f)
40	1000	1020	19.6	19.5	19.5	14 700	0		0.40	0.40	0.41	19.6	1.00	(f)

TABLE 1. Parameters of the experiments with rods of diameter $D = 1.6$ cm: $\rho_{a,c}$ is the density of the ambient/current fluid, g' is the reduced gravity, H is the height of the ambient fluid, h_0 is the height of the current in the lock-release experiments, $q' \equiv q(1 - \kappa)$ is the inflow rate coefficient referred to the 30° sector tank, κ is the density of vegetation, α and γ are constant. γ_{th} is the theoretical value evaluated for $\lambda = 1, 2$, while γ_{exp} is the experimental value. $U = \sqrt{g'H}$ is the velocity scale, $T = H/U$ is the timescale. The symbol in the last column “remark” stands for lock-release (LR), lock-release full depth/partial depth (f/p), constant inflow rate (CF), waxing (WX), and waning (WN) inflow rate, respectively. Note that, in the comparison between experiments and theory, the fact that the volume in eq.(2.6) includes both fluid and vegetation has been taken into account.

s after the lift of the gate, during Exp. 8 in LR, in order to give an overview of the shape of the current propagating radially from the centre. The dense current is red, while the ambient fluid is transparent. The vertical rods tend to overshadow the view, especially on the right-hand side of the images, where the radial distance r is great and the number of rods filling the tank increases. The red colour of the dense current is also not homogeneous, as it gets darker from left to right as the gap of the tank increases from the centre towards the outer radius. In figure 6a, at $t = 0$, the fluid is still at rest inside

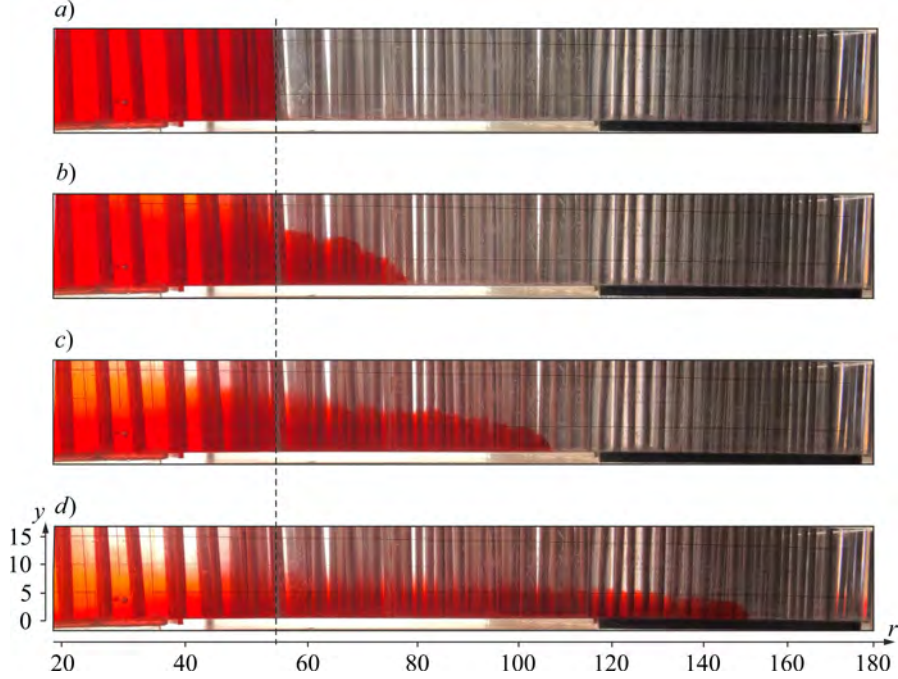


FIGURE 6. *a*)-*d*) Snapshots of the lateral side of the tank taken at $t = 0 - 4 - 8 - 16$ s for Exp. 8, lock-release ($\alpha = 0$). The dashed vertical line indicates the section of the gate. Units are in centimetres. The images are not corrected for distortion.

the lock, but as the gates is lifted, the current starts spreading and its thickness reduces in time. At a short time after the lift of the gate, a significant entrainment of the ambient fluid occurs as the current propagates, as we can see from figure 6*b*, where the lock is still entirely filled by red fluid, but the nose of the current is advancing further. As time goes by, diffusion also occurs at the interface, and the dye appears stratified in concentration in the vertical direction, especially close to the left hand-side of the snapshots, at $r = 0$, see figures 6*c*)-*d*). The red spot on the right hand-side in figure 6*d* is a reflection of the current on the transverse vertical wall.

We observe that the condition $h/H \ll 1$ is not strictly satisfied. It is indeed possible to develop more sophisticated models with two layers, but the mathematical complication (even in Cartesian cases, and much more so in a cylindrical geometry) usually prevents an intuitive solution. There is consensus in the research community that the one-layer model is a valid approximation tool for $h/H < 0.5$, although precise estimates of the magnitude of the error are not available (this is discussed in Ungarish 2020).

Figure 7 shows some snapshots of the lateral view of the tank taken at $t = 6 - 36 - 50 - 60$ s from the time when the pump was switched on, during Exp. 22. In this experiment, the volume inflow rate increases with $Q \propto t^2$, and as Q increases, the height of the current close to the source increases, with more evident billows.

Figure 8 represents snapshots of the Exp. 22 from the top. We can observe that the front of the current is fairly radially symmetric.

In order to gain further insights on the dynamics of these GCs, lateral profiles have been extracted at different times and for different kinds of inflow. Figure 9 shows some dimensional lateral profiles of the current taken at various instants, for an LR experiment (Exp. 5) in figure 9*a*), an increasing influx experiment (Exp. 21) in figure 9*b*), a decreasing

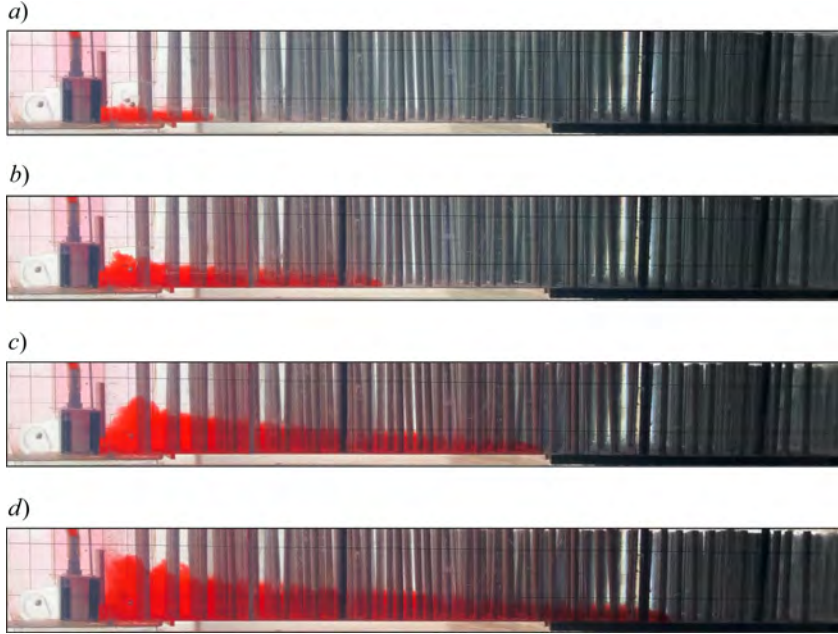


FIGURE 7. *a-d*) Snapshots of the lateral side of the tank taken at $t = 6 - 36 - 50 - 60$ s for Exp. 22 ($\alpha = 3$), waxing inflow rate with $Q \propto t^2$. Images are not corrected for distortion.

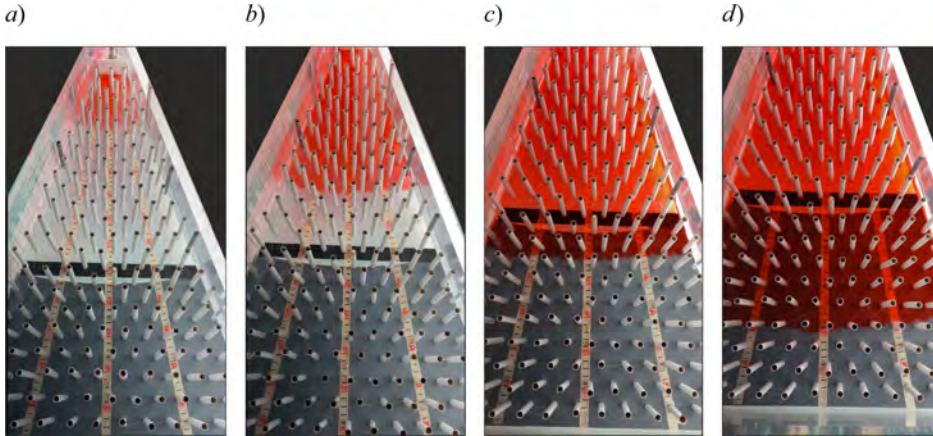


FIGURE 8. *a-d*) Snapshots of the top view of the tank taken at the same times as figure 7, $t = 6 - 36 - 50 - 60$ s during Exp. 22 ($\alpha = 3$), waxing inflow rate with $Q \propto t^2$. Images are not corrected for distortion.

influx experiment (Exp. 28) in figure 9*c*, and a constant influx experiment (Exp. 33) in figure 9*d*. In figure 9*a*, the grey dotted vertical line at $r = 55$ cm marks the position of the gate at $t = 0$, while the grey dotted square at $r = 25$ cm in the other three panels is a schematic for the diffuser, so no data are available for $r < 25$ cm as the current only propagates downstream.

Profile trends are consistent with expectations in all four reported cases. In the proximity of the fluid injection section (which in the experiments is necessarily advanced with respect to the origin of the cylindrical sector) the greatest deviations from the profiles, consistent with the shallow-water scheme of the analytical reference model, are observed.

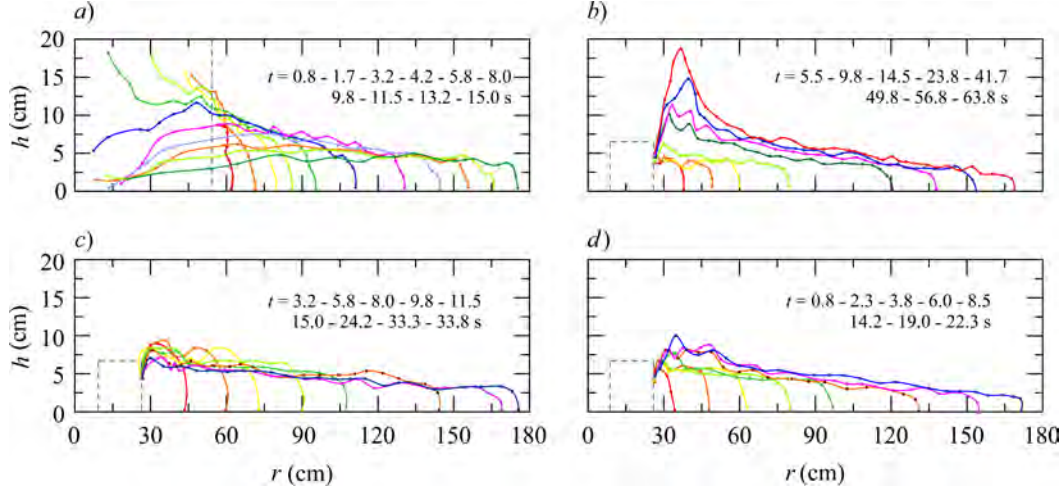


FIGURE 9. Dimensional lateral profiles extracted from images at various instants for *a*) an LR experiment (Exp. 5, $\alpha = 0$); *b*) waxing influx experiment (Exp. 21, $\alpha = 2.5$); *c*) waning influx experiment (Exp. 28, $\alpha = 0.46$); *d*) constant influx experiment (Exp. 33, $\alpha = 1$).

In the case of lock-release (figure 9*a*), the initial acceleration is sufficiently significant to make the inertial contribution dominant with respect to the drag of the vegetation. However, the decay of the inertial stage is fast due to the effect of vegetation and also because of the interaction with the ambient fluid, which in the region of the lock has a significant velocity and opposite to that of the current: it results in a very high shear with the formation of billows and entrainment of ambient fluid, and a consequent mixing.

As the front advances toward the periphery of the circular sector, the fluctuations at the interface between the dense current and the ambient fluid are damped, as the current front widens and the average velocity is reduced. The thickness of the current is reduced, and the dynamics appears more adherent to that of the interpretative model. An important difference, due to the presence of vegetation, is the scale of the turbulence, which is necessarily controlled also by the downstream wake of the cylinders. The mixing processes appear amplified, and consequently the interface between dense current and ambient fluid is less defined than in the case of the absence of vegetation.

For GCs with increasing flow rate over time (figure 9*b*), near the inlet section the turbulence level increases over time, creating an accumulation of denser fluid that originates a progressively increasing pressure gradient. The region with very different characteristics of the flow field and of the current, compared to the theoretical model, becomes progressively larger, even if the current, moving away from this region, appears to follow the theoretical model hypotheses. On the contrary, in the case of current with waning flow rate (figure 9*c*), the flow characteristics appear sufficiently smooth, with a progressive reduction, in time, of the thickness near the inlet section.

Last, currents generated by a constant inflow rate (figure 9*d*) reach a substantial equilibrium after a short time, with a current profile that, while fluctuating, remains essentially unchanged over time and with a modest reduction in the average interface slope.

By sampling in the vertical the dense current with a syringe, with the methodology described in §3, we checked that the currents undergo a strong reduction in density while propagating, and are also stratified in the vertical direction. For example, in Exp. 33, while $\rho_c = 1100 \text{ kg m}^{-3}$ in the container from where the pump takes fluid, the density

decreases to $\rho_c = 1048 \pm 4 \text{ kg m}^{-3}$ at the bottom and $\rho_c = 1033 \pm 3 \text{ kg m}^{-3}$ just below the density interface. This is a result of a great entrainment of the light ambient fluid into the GC. The amount of entrainment was also evaluated by comparing the volume injected in the tank with the volume of the current estimated from the lateral profiles in time. We found that the volume estimated with the last technique was double the injected volume, almost uniformly during the current propagation. This dilution of the current by a factor of 2 was also found by Hatcher *et al.* (2000), who stated that the mixing occurs for a few seconds after releasing the gate. They also suggest that the total buoyancy of the flow, given by the product of $g'q$ is conserved during the flow, so if a reduction of g' occurs due to dilution, an increase in the value of q compensates and the behaviour of the nose position is unaffected. We will verify this later on.

We now compare some experimental lateral profiles with the theoretical predictions in figure 10, where the theoretical height of current h is scaled with respect to a reference height h_{ref} , here set as $h_{ref} = h(y = 0.2)$, and is shown as a function of the non-dimensional radial coordinate $y = r/r_N$. The choice of a reference section that differs, as would be natural, from the axis of the cylinder sector (i.e. with the origin of the chosen radial coordinate system), derives from the approximations of the physical model, which requires adequate space for the lock, or for the diffuser. From a mathematical point of view, the origin also generates a singularity. The results are little affected by the exact position of the reference section.

Figure 10a refers to an LR experiment ($\alpha = 0$, Exp. 8 in table 1), while figure 10bcd refers to constant inflow rate experiments (CF $\alpha = 1$, Exp. 17), waxing inflow rate WX with $\alpha = 3$, Exp. 22, and waning inflow rate $\alpha = 0.45$, Exp. 27 in table 1 respectively). The vertical error bars are smaller than the size of the symbol and are not shown. The experimental and theoretical results show a variegated behaviour, especially at late times when the self-similar solution is reached. In figure 10c, at $y = 0.2 - 0.3$, the experimental data showing the engulfment of ambient fluid in the dense current at high Q , depart from the theoretical behaviour. This is consistent, as the SW model does not include mixing and entrainment. In addition, the nose of the current ($y = 1$) has a shape different from the shape predicted by the theory. This is more evident when $\alpha = 3$, see figure 10c, than for experiments with smaller α , see figure 10ab. This can be attributed to viscosity, which becomes more relevant at low flow rates, with a corresponding lower front speed. The experimental front Reynolds number is systematically quite small. In figure 10d, which refers to a waning inflow experiment, the experimental data differ significantly from the theoretical prediction, especially for $y > 0.5$. The first reason may stand in some technical issues related to the injection of fluid in the tank at early stage. The pump used in the present study works well between 20 and 500 mls^{-1} , so a strong linear increase in the inflow rate was imposed by the LabView software for the first few seconds, in order to let the pump reach the full scale value. Then, the pump followed the fixed waning inflow rate law. This early strong injection may have led to a significant accumulation of fluid at the nose of the current. The thickness of the nose is then much larger than zero. Another reason for the difference between experimental data and theoretical predictions may stand in the radial extent of the tank, which could be non-sufficient for the self-similarity to be reached in the waning inflow rate conditions.

Figure 11 shows the time series of the non-dimensional position of the nose of current. The experiments are separated into three plots, and the experiments in each plot are separated into two-three groups for an easy visualization of the results. The data are subjected to a vertical shift, which has no influence on the slope of the fitting lines. The solid lines represent the theoretical slope $\gamma = (\alpha + \lambda)/(3 + \lambda)$, evaluated for $\lambda = 2$.

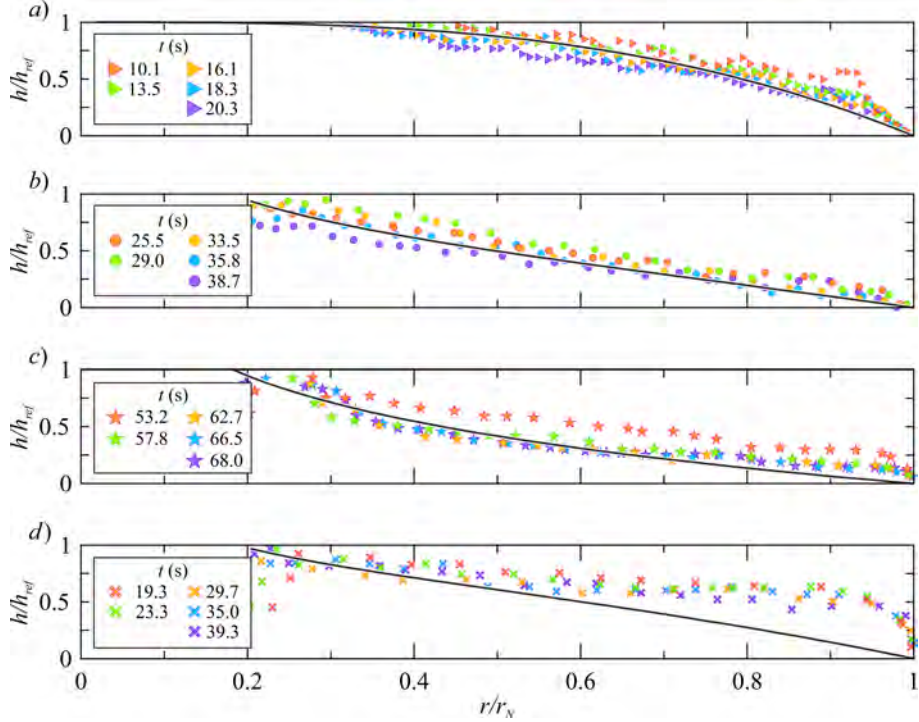


FIGURE 10. Lateral profiles of the current at different times for *a*) a lock-release experiment, $\alpha = 0$, Exp. 8, *b*) a constant inflow experiment, $\alpha = 1$, Exp. 17, *c*) a waxing inflow experiment, $\alpha = 3$, Exp. 22, and *d*) a waning inflow experiment, $\alpha = 0.45$, Exp. 27. The solid black lines refer to the theoretical similarity solution, when $\lambda = 2$ scaled with h_{ref} .

Figure 11*a* refers to the LR experiments without vegetation (Exp. 1–4, $\kappa = 0$) and with vegetation (Exp. 5–10) and CF experiments with $\kappa = 0.050$ (Exp. 11–19) and $\kappa = 0.081$ (Exp. 31–34). Experiments without vegetation were run to check the overall quality of the experimental apparatus in a simple configuration. For all tests, the asymptotic trend appears significantly consistent with the theoretical slope, with varying times (lengths) of adaptation but with a remarkably large portion of the path characterized by linear trend (in loglog scale). This confirms that the front propagation is not affected by mixing and dilution of the current during propagation, as also suggested by Hatcher *et al.* (2000). No appreciable difference is perceived as areal density of vegetation varies. The agreement is also for the four initial experiments without vegetation, where the exponent equals the theoretical value 0.5 as predicted in Ungarish (2009).

Figure 11*b* refers to increasing (waxing) inflow experiments (Exp. 20–25), where the different inclinations are related to various exponents of the inflow rate function. Again, the theory reproduces the experiments with adequate correctness, although for Exp. 20–21 the asymptotic velocity is closer to the value that pertains to $\lambda = 1$ than to $\lambda = 2$.

Figure 11*c* refers to decreasing (waning) inflow experiments (Exp. 27–30). In all four experiments, the front theoretical velocity is systematically in defect of the experimental velocity. The experimental slope is around 0.6, 10–26% greater than the theoretical values of 0.55–0.49 predicted when $\alpha = 0.76–0.45$ respectively. This modest agreement between theory and experiments was most visible in the side profiles. It is evident that the buoyancy of the GC appears to be influenced, starting from the profile near the

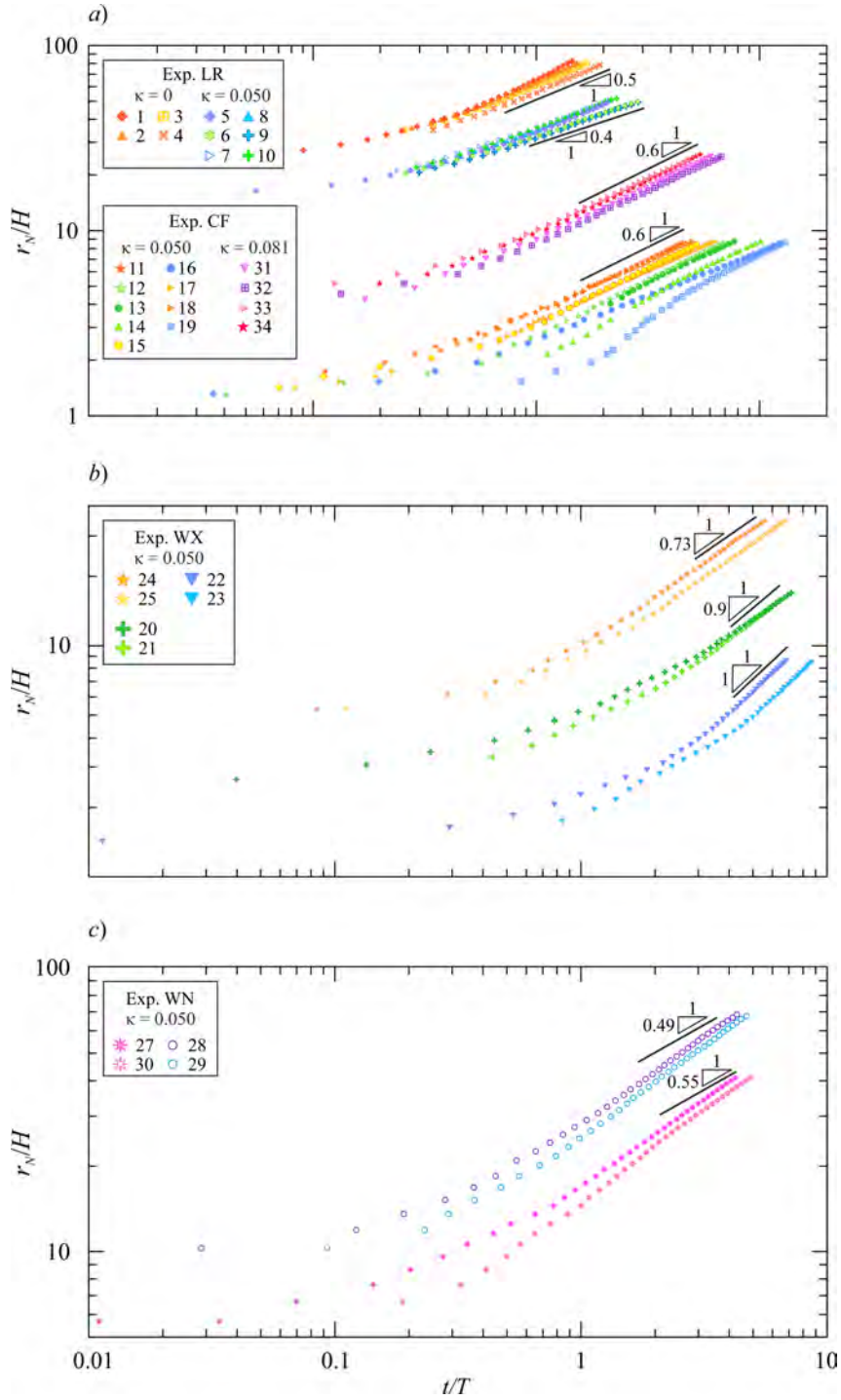


FIGURE 11. Non-dimensional position of the nose of the current as a function of the non-dimensional time *a*) for lock-release experiments with $\kappa = 0$ (LC Exp. 1 – 4), $\kappa = 0.050$ (LC Exp. 5 – 10), constant influx experiments with $\kappa = 0.050 - 0.081$ (CF Exp. 11 – 19 and CF Exp. 31 – 34); *b*) for increasing influx (WX, Exp. 20 – 25, $\kappa = 0.050$), and *c*) for decreasing influx (WN Exp. 27 – 30, $\kappa = 0.050$). The slope of the black solid lines represents the theoretical power γ computed for $\lambda = 2$. The slope for Exp. 1 – 4 refers to the theoretical analysis in Ungarish (2009).

front, by the secondary effects of mixing, resulting in an increase in apparent thickness and also in a different front velocity. A second possible reason, already mentioned before, is that the experimental apparatus is not long enough for the current to reach the self-similarity. We should note here that the self-similar solution requires an adjustment time and remains for a limited time, in the spirit of Barenblatt's self-intermediate asymptotic: in a first phase the system adjusts and gradually forgets the initial conditions; in a second phase it conforms to the self-similar solution; in a third phase it departs again from the self-similar condition because of perturbations that amplify, or because the assumptions of the model fail. In order for the solution obtained in turbulent drag-buoyancy balance to be applicable, it is also necessary that $t_{v1} < t < t_c$, as detailed in § 2.

The theoretical behaviour of the radial velocity u along the radial coordinate r/r_N and computed for $\lambda = 2$ is used to estimate the Reynolds number $Re = uh/\nu$ (h is the measured depth of the current, ν is the kinematic viscosity almost constant and equal to the fresh water value) shown in the left column in figure 12 for a lock-release experiment (LR Exp. 5) in panel a), waxing influx experiment (WX Exp. 21) in panel b), waning influx (WN Exp. 28) in panel c) and constant influx (CF Exp. 33) in panel d). Panels e-f-g-h) in the right column refer to the same experiments and show the Reynolds number of the vegetation $Re_{rod} = ud/\nu$, where u is the theoretical velocity of the current.

In all these plots, the value of $\lambda = 2$ has been assumed, but although the current is in a turbulent regime for much of its development, except near the front, the resistance of the vegetation is in general less than that competing to $\lambda = 2$, since Re_{rod} is less than 3000. For lock-release experiments, the initial phase is characterized by fully developed turbulence of both the current scaled with its depth and scaled with the rods diameter. This behaviour recurs in a large portion of the current near the front, even in the later stages, while the turbulence decays and the resistance of the rods scales with $\lambda < 2$ in the residual portion of the current, starting from the lock section. This justifies the good agreement of the theoretical model, which refers to a constant value of λ . In all other cases, although the value of the velocity remains fairly uniform with r/r_N , the level of turbulence of the current appears to be variable, and furthermore, on the basis of Re_{rod} , we expect a value of $\lambda < 2$.

We observe that the front position is better reproduced by the model than the height profile of the currents. In fact, the front position scales with gg' , see eq.(2.32), and the total buoyancy is preserved.

5. Conclusion

We experimentally studied the propagation of radially symmetric GCs in the presence of drag due to vegetation. A complementary part of the experimental work was concerned with the measurement of drag, which allowed us to estimate the λ exponent of the velocity power law that expresses the drag on the propagation of the GC.

The exponent λ of the drag $\propto V^\lambda$ increases with Re_{rod} and tends to 2 for $Re_{rod} \gg 3000$. The transition is a function of κ , although the results of tests performed with only two values of this density cannot be sharp. Two additional sets of drag measurements with smaller diameter rods, with the same density, indicate that drag varies with D , with $\tilde{c} \propto (\kappa/D)^2$ and $\tilde{c} \propto (\kappa/D)$ for $\lambda = 1, 2$ for small κ ; however, this variability only quantitatively affects the results, leaving unchanged the structure of the model, with the same asymptotic value for λ . Scaling drag measurements with the velocity in the constricted section, instead of the apparent velocity, improves the collapse of drag coefficients to a unique universal value.

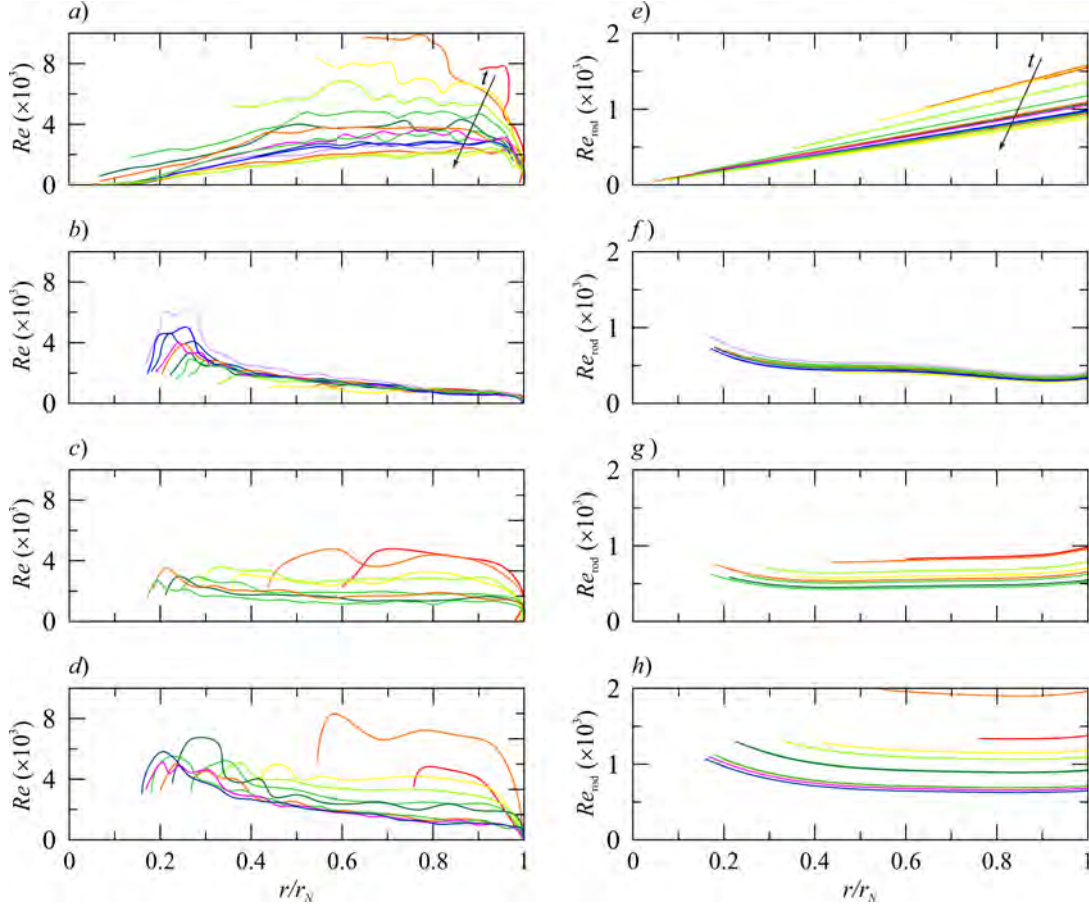


FIGURE 12. Profiles of the $Re = uh/\nu$ (left column) and $Re_{rod} = ud/\nu$ (right column) against the radial coordinate r/r_N for a)-e) lock-release experiment (Exp. 5, $\alpha = 0$); b)-f) waxing influx (Exp. 21, $\alpha = 2.5$); c)-g) waning influx (Exp. 28, $\alpha = 0.46$), and d)-h) constant influx (Exp. 33, $\alpha = 1$). Re is computed with u from theory with $\lambda = 2$ and h from experiments, Re_{rod} is computed with u from theory with $\lambda = 2$.

In order to analyse the variety of conditions under which the most dense fluid is injected, we conducted experiments with GCs produced by lock-release (constant volume), and also with GCs sustained by an influx that is either constant, increasing or decreasing in time. The analysis of the lateral profile of the current and the position of the front in time provide useful information for the classification of the pattern of the flow field. For all four cases, the current tends to become self-similar, with an asymptotic front speed that is reproduced quite well by a simple shallow-water one layer model. In detail, the accuracy of the predictions is better for the lock-release tests, and is not so good for GCs sustained by waning flow rate. The reason is not the deficiency of the theoretical model, but rather the difficulty to specify precisely the conditions at the influx position.

In order to get an estimate of the level of turbulence triggered by the floor of the tank and by the rods (this last one gives an estimate of the value of λ), we calculated the Reynolds number of the current, with a geometric scale equal to the measured local depth, and the Reynolds number of the vegetation, with a geometric scale equal to the diameter of the rods. The current velocity was taken from the theoretical model. The result is that for lock-release the current is almost always turbulent and $Re_{rod} > 3000$,

i.e. $\lambda = 2$; for the other tests the regime is viscous for more or less extended portions of the current and $Re_{\text{rod}} < 3000$, without homogeneity. Such indications motivate the experimental behaviour of currents, point to the causes of deviations from models, and shed light on the more detailed aspects that deserve attention in more sophisticated models.

The theoretical analysis that predicts a self-similar flow and propagation with t at constant power, has been applied to currents that do not strictly or always meet the assumptions of the model, and hence the question of agreement and reliability is relevant. The experimental results indicate that some elements of self-similarity are still satisfied even if there are significant quantitative deviations in other aspects: the velocity of the current, for example, after a preliminary adaptation, becomes self-similar, but the experimental exponent in $r_N \sim t^\gamma$ is slightly different from the theoretical one; the differences can be attributed to the elements of the process that have not been deliberately included, first mixing and entrainment. Other variables, such as current depth, take on different values from the experiments (this is the case with waning flow rate currents), but the experiments still indicate a self-similar profile. We think that this is an encouraging insight of our experimental study. The theoretical model makes some bold simplifications, but it turns out that the associated effects make only a small contribution to the overall behaviour of the current. It is as if the self-similar solution is extremely stable even in the presence of strong disturbances, albeit with slightly different scaled variables than the theoretical model. This behaviour was already known and described with reference to the initial and boundary conditions, which are soon “forgotten” by the current, reaching a self-similar regime sooner or later. (We note in passing that the attainment of self-similarity may be reached for some non-circular lock geometries, see Zgheib *et al.* 2015, although without reaching axisymmetric shape and hence without forgetting the initial asymmetry). It was instead less known with reference to the general structure of the flow field, which on an experimental basis and for the present set-up tends anyway towards a self-similar regime.

As an extension of the analysis, the parameterisation of mixing and entrainment processes and their involvement in the model is suggested. It is likely that the analytical structure leading to self-similarity of the first-kind will be lost due to the introduction of new scales in the process. Something similar has already been addressed, for example in Hogg *et al.* (2000) and in Di Federico *et al.* (2017), and solved with perturbation techniques. Possibly, a second-kind self-similarity arises, where a power-law dependence of the variables is retained but with the exponents represented by eigenvalues of the differential problem.

Appendices

A. Drag measurements for different rods diameter and scaling rules

An additional set-up was built in order to measure the drag coefficient of a set of rods, attached to a wooden panel, with density $\kappa = 0.050 - 0.081$ and with two different diameters of the rods, arranged in order to keep constant the density while reducing the distance between two neighbour rods. The drag analysis was extended beyond what was strictly necessary for the experimental study of the GCs in our experiments, in order to quantify the joint effect of density and diameter of the rods. The wooden panel with the rods was positioned inside a rectangular channel, as illustrated in figure A.1. The channel was filled with water up to $h = 19.9$ cm, so that the rods were almost entirely immersed in the fluid. A tension load cell was put at the top of the panel in order to measure the

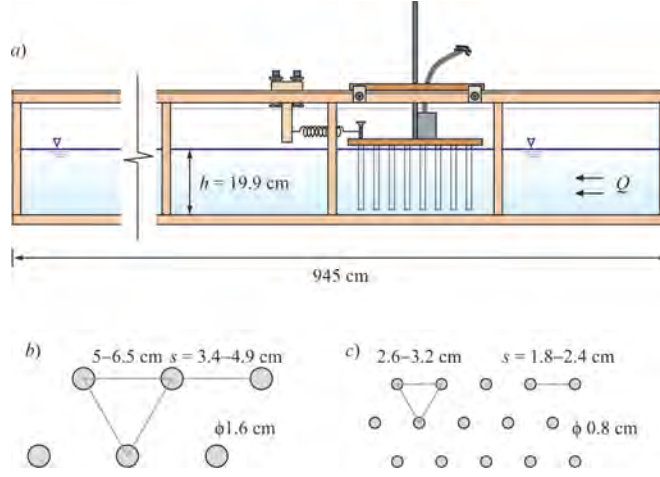


FIGURE A.1. Experimental set-up for the drag measurement. *a)* Side view of the channel with the panel supporting the rods and the load cell; *b)* plan view of the 1.6 cm diameter rods and *c)* of the 0.8 cm diameter rods.

Pattern no.	Rods diameter D (cm)	Rods spacing s (cm)	No. of rods per unit area N (m^{-2})	Rods density κ	Frontal area per unit volume a (cm^{-1})
1	1.6	4.9	237	0.050	0.066
2	1.6	3.4	392	0.081	0.138
3	0.8	2.4	982	0.050	0.138
4	0.8	1.8	1464	0.081	0.247

TABLE A.1. Arrangements of varying rods concentration and diameter $D = 1.6 - 0.8$ cm. a is the frontal area per unit volume.

drag force F of the set of rods, when crossed by different values of volume inflow rates Q , hence by water flowing at different horizontal velocity V . The tension load cell was previously calibrated with a dynamometer with an accuracy of 0.01 N in the same set-up configuration but in air. A spring slightly pulled the panel at the downstream side of the panel in order to apply a pre-tension to the load cell and let the measurements fall within the instrumental range of the dynamometer, eliminating the dead band.

Table A.1 lists the main parameters of the two patterns with two different diameters of the rods for the drag force measurements, which for the diameter $D = 1.6$ cm correspond to the patterns adopted for the GCs experiments documented in the main body of this manuscript.

Figure A.2*ab* shows the drag force measurements as function of V (top axis) and of Re_{rod} (bottom axis) for the set of rods with density $\kappa = 0.050$ and 0.081 respectively and diameter 1.6 cm. The module of the drag force for a generic body can be expressed as

$$F = \frac{1}{2} C_D \rho A V^2 = K_D |V|^\lambda, \quad (\text{A.1})$$

where C_D is the average drag coefficient, ρ is the fluid density and A is the frontal area of the body, V is the apparent velocity (defined as the discharge in the rod layer over

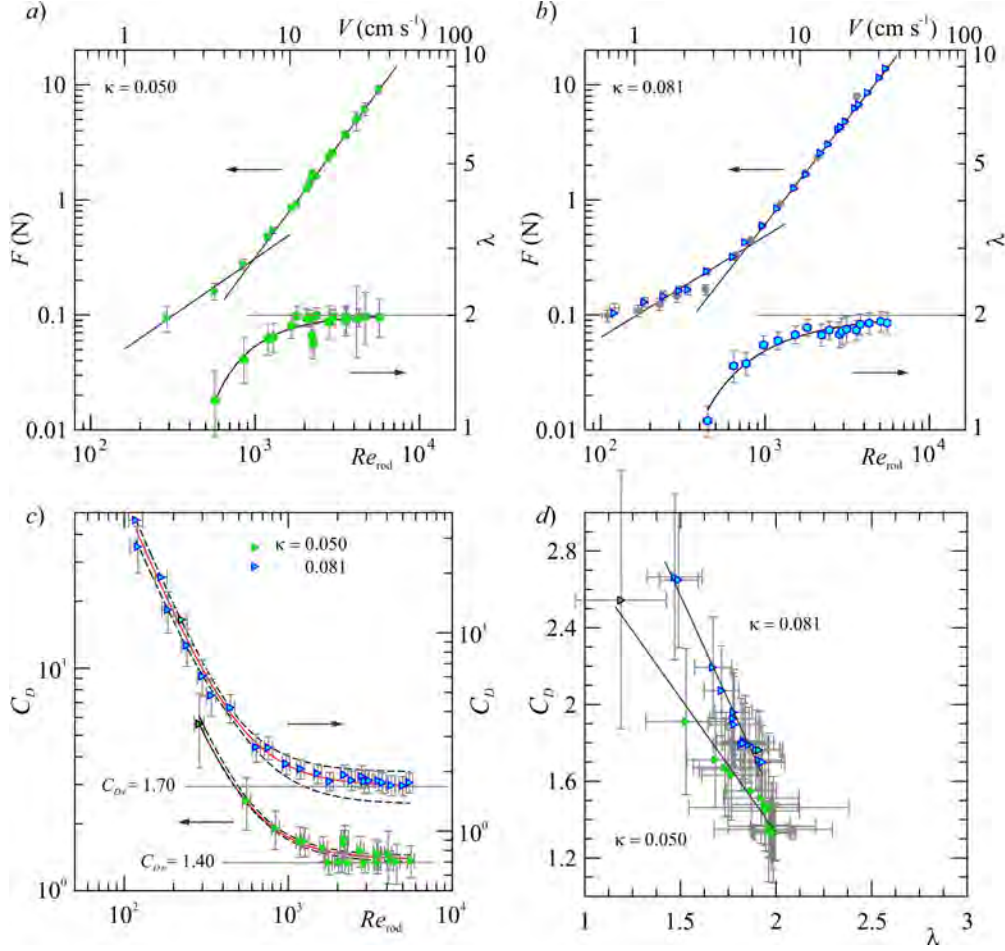


FIGURE A.2. Drag measurements for 1.6 cm diameter rods. *a*) Drag force F for $\kappa = 0.050$, and *b*) for $\kappa = 0.081$ (the grey squares are a test of reproducibility of drag measurement after two months from the test visualised with blue triangles) and λ referred to the right axis; *c*) the drag coefficient C_D as a function of the Reynolds number Re_{rod} , with different vertical axis for an easy visualisation; *d*) the drag coefficient as a function of λ . The dashed curves are the 95% confidence limits, error bars indicate one standard deviation.

the gross cross-sectional area) and $Re_{rod} = VD/\nu$, where D is the diameter of the rod and ν is the kinematic viscosity of water, assumed equal to $10^{-6} \text{ m}^2 \text{ s}^{-1}$.

In our experiments, $A = nA_r$, where $n = 36 - 55$ is the number of 1.6 cm diameter rods ($n = 126 - 210$ for the 0.8 cm diameter rods) attached to the panel for $\kappa = 0.050 - 0.081$ respectively, and A_r is the frontal area of a single rod covered by water, equal to $A_r = D l_s$ with l_s the submerged length of the rod.

Figure A.2c shows the drag coefficient as a function of Re_{rod} , with vertical error bars computed by propagating in quadrature the uncertainties of the involved variables:

$$\frac{\Delta C_D}{C_D} = \sqrt{\left(\frac{\Delta F}{F}\right)^2 + \left(\frac{\Delta \rho}{\rho}\right)^2 + \left(\frac{\Delta D}{D}\right)^2 + \left(\frac{\Delta l_s}{l_s}\right)^2 + 4\left(\frac{\Delta V}{V}\right)^2}, \quad (\text{A.2})$$

where l_s is the submerged height of the rods. The main contribution to uncertainty is due to velocity estimation and to force measurement. In fully turbulent flows, the drag

coefficient is constant. On the other hand, in transitional and viscous regime the drag coefficient depends on the fluid velocity and on κ .

We can identify two different regimes where the drag force $\sim V$ for $Re_{\text{rod}} < 3000$ and $\sim V^2$ for $Re_{\text{rod}} > 3000$. This is a classical result valid for internal and external flows, with the drag coefficient proportional to the inverse of the Reynolds number in the viscous regime, and independent of the Reynolds number in the asymptotic turbulent regime, at high Reynolds number (asymptotic independence of turbulence from viscosity). For the experiments with $\kappa = 0.050$ the regression analysis of the experimental data for $D = 1.6$ cm gives

$$\begin{cases} F \approx 5.1 \cdot 10^{-2} Re_{\text{rod}}^{0.99} \text{ N} & \text{for } Re_{\text{rod}} < 3000, \\ F \approx 9.2 \cdot 10^{-3} Re_{\text{rod}}^{1.94} \text{ N} & \text{for } Re_{\text{rod}} > 3000, \end{cases} \quad (\text{A.3})$$

respectively. The results are similar for $\kappa = 0.081$.

If we calculate the logarithm of eq.(A.1) and then differentiate, we obtain

$$\frac{d \ln F}{d \ln V} = \frac{dF/dV}{F/V} = \lambda. \quad (\text{A.4})$$

Figure A.2ab shows the values of λ (filled circles) referred to the right vertical axis. The regression functions are

$$\begin{cases} \lambda = 2 - 1.2 \cdot 10^4 Re_{\text{rod}}^{-1.5} & \text{for } \kappa = 0.050, \\ \lambda = 2 - 4.3 \cdot 10^2 Re_{\text{rod}}^{-1} & \text{for } \kappa = 0.081. \end{cases} \quad (\text{A.5})$$

Figure A.2c shows the drag coefficient C_D derived from equation A.1, as a function of Re_{rod} for $\kappa = 0.050-0.081$ respectively. For both values of κ , we can observe a progressive transition towards the asymptotic drag coefficient. The interpolating curves are

$$\begin{cases} C_D = 1.40 + 2.3 \cdot 10^5 Re_{\text{rod}}^{-1.9} & \text{for } \kappa = 0.050, \\ C_D = 1.70 + 5.1 \cdot 10^5 Re_{\text{rod}}^{-2} & \text{for } \kappa = 0.081. \end{cases} \quad (\text{A.6})$$

The drag increases with κ and assumes the asymptotic value $C_{D\infty} = 1.40 \pm 0.10$ and $C_{D\infty} = 1.70 \pm 0.10$, for $\kappa = 0.050 - 0.081$, respectively. Regarding the dependence of the drag coefficient on Reynolds number and, more generally, on the characteristics of the flow field and of the vegetation, Vargas-Luna *et al.* (2016) indicate that the drag of the vegetation is a function of other variables as well. In this respect, the structure of eq.(A.6) is an approximation. Figure A.2d shows C_D versus λ , with the drag coefficient decreasing linearly with the value of λ .

A similar analysis was conducted for rods with $D = 0.8$ cm. The interpolating curves are

$$\begin{cases} C_D = 1.20 + 2.8 \cdot 10^2 Re_{\text{rod}}^{-1} & \text{for } \kappa = 0.050, \\ C_D = 1.40 + 6.2 \cdot 10^5 Re_{\text{rod}}^{-2.5} & \text{for } \kappa = 0.081, \end{cases} \quad (\text{A.7})$$

with asymptotic values $C_{D\infty} = 1.20 \pm 0.10$ and $C_{D\infty} = 1.40 \pm 0.10$ for $\kappa = 0.05 - 0.081$ respectively. These values are very similar to those calculated for rods of diameter 1.6 cm. Figure A.3 shows λ and C_D as a function of Re_{rod} for $\kappa = 0.050 - 0.081$ and for $D = 1.6 - 0.8$ cm.

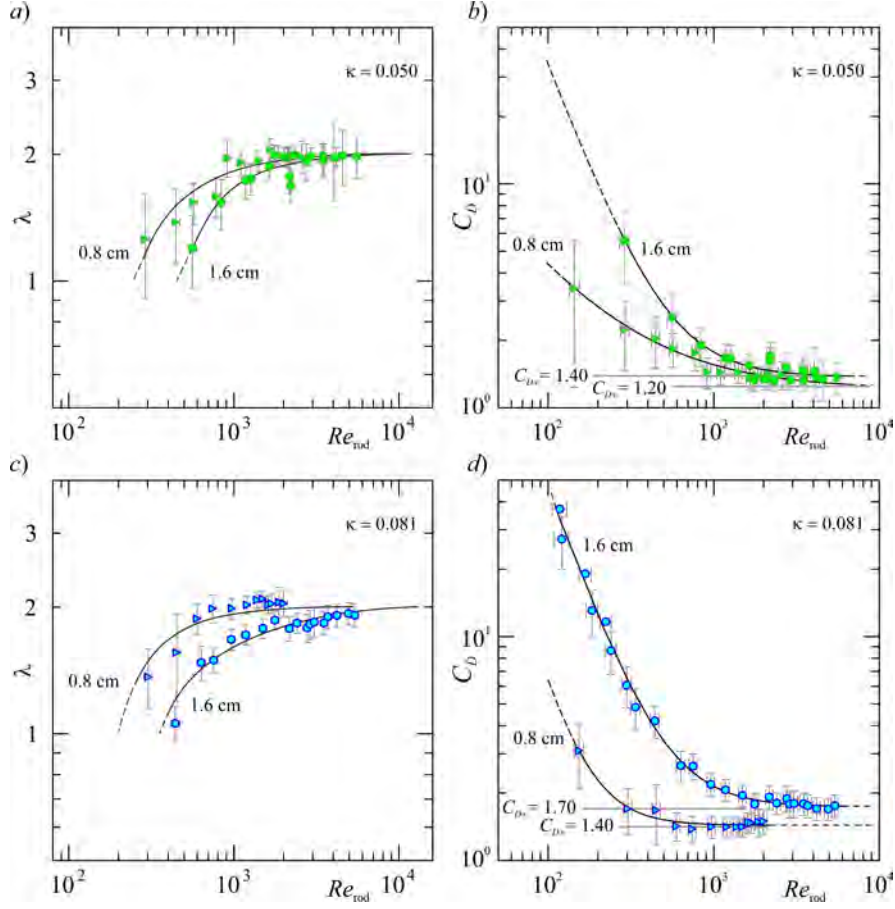


FIGURE A.3. Comparison of drag measurements for 1.6 and 0.8 cm diameter rods. *a)* Exponent λ and *b)* drag coefficient for $\kappa = 0.050$ as a function of Re_{rod} ; *c)* and *d)* same variables for $\kappa = 0.081$. Curves are the interpolating functions, error bars refer to one standard deviation.

From the definitions results that the drag contribution term is

$$\tilde{c}|V|^\lambda = \frac{F}{\rho b l l_s}, \quad (\text{A.8})$$

where b is the channel width, l is the streamwise length of the support of the rods and l_s is the height of the rods, almost equal to the water depth. Figure A.4*ab* shows the experimental values and the interpolating curves of the coefficient \tilde{c} and of λ .

The interpolating functions for \tilde{c} are sigmoids with expression for $D = 1.6 - 0.8$ cm

$$\begin{cases} \tilde{c} = \frac{0.053}{0.0187 + \exp(-0.0037 Re_{\text{rod}})} m^{1-\lambda} s^{\lambda-2} & \text{for } \kappa = 0.050, \\ \tilde{c} = \frac{0.108}{0.0281 + \exp(-0.0041 Re_{\text{rod}})} m^{1-\lambda} s^{\lambda-2} & \text{for } \kappa = 0.081. \end{cases} \quad (\text{A.9})$$

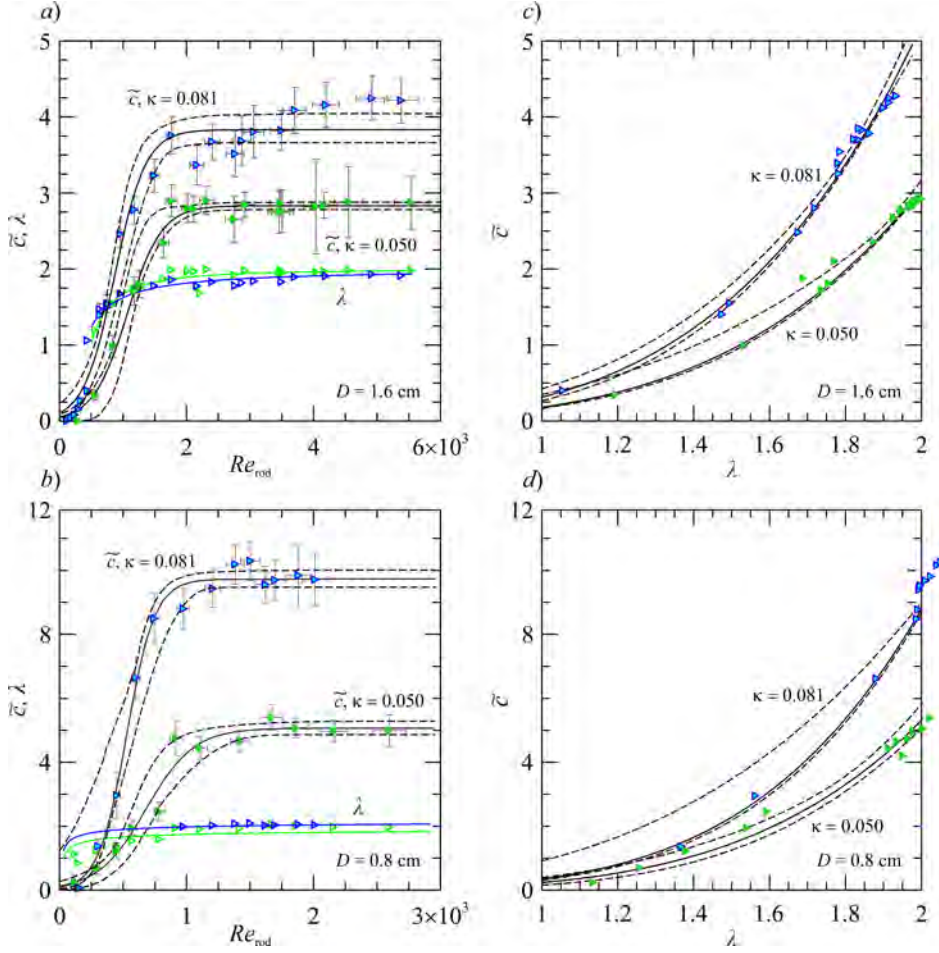


FIGURE A.4. Drag measurements for 1.6 cm and 0.8 cm diameter rods. *ab*) Coefficient \tilde{c} (filled symbols) and λ (open symbols) as a function of Re_{rod} for $\kappa = 0.050 - 0.081$, and *cd*) coefficient \tilde{c} as a function of λ for $\kappa = 0.050 - 0.081$, with $\tilde{c} \propto \lambda^{\approx 4}$. Curves are the interpolating functions, error bars and confidence bands refer to one standard deviation.

and

$$\begin{cases} \tilde{c} = \frac{0.134}{0.0265 + \exp(-0.0053Re_{\text{rod}})} m^{1-\lambda} s^{\lambda-2} & \text{for } \kappa = 0.050, \\ \tilde{c} = \frac{0.082}{0.0084 + \exp(-0.0091Re_{\text{rod}})} m^{1-\lambda} s^{\lambda-2} & \text{for } \kappa = 0.081. \end{cases} \quad (\text{A.10})$$

The asymptotic values corresponding to $\lambda = 1, 2$ for $D = 1.6 - 0.8$ cm are equal to

$$\begin{cases} \tilde{c} = 0.18 \text{ s}^{-1}; \tilde{c} = 3.06 \text{ m}^{-1} & \text{for } \lambda = 1, 2, \kappa = 0.050, \\ \tilde{c} = 0.31 \text{ s}^{-1}; \tilde{c} = 5.19 \text{ m}^{-1} & \text{for } \lambda = 1, 2, \kappa = 0.081. \end{cases} \quad (\text{A.11})$$

Pattern no.	D (cm)	κ	$\lambda = 1$			$\lambda = 2$		
			\tilde{c} (s^{-1})	exp.	$r_{\tilde{c}}$ theory	\tilde{c} (m^{-1})	exp.	$r_{\tilde{c}}$ theory
1	1.6	0.050	0.18	1	1	3.06	1	1
2	1.6	0.081	0.31	1.72	4.19	5.19	1.70	1.67
3	0.8	0.050	0.23	1.28	7.41	5.34	1.75	2.00
4	0.8	0.081	0.26	1.44	10.25	8.84	2.89	3.35

TABLE A.2. Experimental values of \tilde{c} for the four drag measurements tests in the limiting cases of $\lambda = 1, 2$. There is a comparison between the experimental ratio $r_{\tilde{c}}\text{-exp.}$ and theoretical scaling $r_{\tilde{c}}\text{-theory}$ indicated by eq.(A.15), by assuming pattern no. 1 as reference and $r_{\nu} = 1$.

and

$$\begin{cases} \tilde{c} = 0.23 \text{ s}^{-1}; \tilde{c} = 5.34 \text{ m}^{-1} & \text{for } \lambda = 1, 2, \kappa = 0.050, \\ \tilde{c} = 0.26 \text{ s}^{-1}; \tilde{c} = 8.84 \text{ m}^{-1} & \text{for } \lambda = 1, 2, \kappa = 0.081. \end{cases} \quad (\text{A.12})$$

Figure A.4 shows the experimental values and the interpolating curves of the coefficient \tilde{c} and of λ .

Flow within the rods and porous structures is opposed by a viscous resisting force $\propto V$ and form drag $\propto V|V|$, as derived from the Forchheimer equation (Whitaker 1996); the former is a function of the permeability K , which is controlled by the internal geometry of the medium, the latter is a function of a dimensional drag coefficient χ controlled again by the internal geometry of the medium. In the present model, a single monotonic expression is adopted, with a resisting force $\propto V|V|^{\lambda-1}$ and $\lambda \in [0, 1]$. There are several models to relate K and χ to the properties of the medium, and a scaling for drag can be obtained following the model proposed by Macdonald *et al.* (1979), who on the basis of data from numerous experiments with a variety of materials, including cylinders, proposed a variant of the Ergun equations (Ergun 1952), with the permeability expressed as

$$K = \frac{D_{eq}^2(1-\kappa)^3}{a_0\kappa^2} \rightarrow \tilde{c}|_{\lambda=1} = \frac{\nu(1-\kappa)}{K} \equiv \frac{a_0\nu\kappa^2}{D_{eq}^2(1-\kappa)^2}, \quad (\text{A.13})$$

and the dimensional coefficient χ expressed as

$$\chi \equiv \tilde{c}|_{\lambda=2} = \frac{b_0\kappa}{D_{eq}(1-\kappa)}; \quad (\text{A.14})$$

a_0 and b_0 are empirical constants and D_{eq} is an equivalent mean sphere diameter ($D_{eq} = 6W_p/A_p$ being W_p and A_p the volume and the surface area of the particles) equal to $1.5D$ for a cylinder.

The scaling rules for $\tilde{c}|_{\lambda=1}$ and for $\tilde{c}|_{\lambda=2}$ for small κ are (Longo 2021)

$$r_{\tilde{c}(\lambda=1)} = \frac{r_{\nu}r_{\kappa}^2}{r_D^2r_{(1-\kappa)}^2}, \quad r_{\tilde{c}(\lambda=2)} = \frac{r_{\kappa}}{r_Dr_{(1-\kappa)}}, \quad (\text{A.15})$$

where r_{ν} , $r_{\tilde{c}}$, r_{κ} , $r_{(1-\kappa)}$ and r_D are the ratio between the values of ν , \tilde{c} , κ , $(1-\kappa)$ (the porosity) and D of two different patterns.

Table A.2 lists the experimental results of \tilde{c} for the four drag measurements tests with two different diameters and density of the rods. The values of the ratio $r_{\tilde{c}}$ are also listed as computed with the experimental data and with eq.(A.15), with pattern no 1 assumed

as reference. The agreement between theory and experiments is quite strong (differences within 15%) for the case $\lambda = 2$, also considering that the agreement found by Macdonald *et al.* (1979) with eqs.(A.13-A.14) was within $\pm 50\%$ for all the experimental data considered, if $a_0 = 180$ and $b_0 = 1.8$. The agreement for laminar flow is less evident, although the increment of \tilde{c} with κ is correctly reproduced. The latter discrepancy was expected, since the number of data and the accuracy of measurements in the viscous regime is lower than in the turbulent regime.

The relevant result for the present drag measurements is that the asymptotic value of λ is unaffected by the rods diameter, although the transitions from the viscous drag regime to the turbulent drag regime and drag values are affected. For small κ it results that $\tilde{c} \propto (\kappa/D)^2$ and $\tilde{c} \propto (\kappa/D)$ for $\lambda = 1, 2$ respectively.

A more in-depth analysis aims to identify the appropriate variables to be adopted to express drag, towards a single expression valid for possible combinations of porosity and obstacle arrangement. Stone & Shen (2002) have suggested expressing the drag in terms of the average velocity at a constricted section, V_c , in the rods, defined by Whitaker (1996) the “intrinsic average” velocity as opposite to the “superficial average” velocity. The velocity V_c can be computed from the superficial velocity (defined as the discharge in the rod layer over the gross cross-sectional area) with the following equation (see Stone & Shen 2002):

$$V_c = \frac{V}{1 - D\sqrt{N}} \equiv \frac{V}{1 - \sqrt{4\kappa/\pi}}, \quad (\text{A.16})$$

where N is the number of rods per unit area. Figure A.5 shows the same variables already presented in figure A.3 but referred to V_c . The asymptotic values of the drag coefficients are more uniform than the data referred to the apparent velocity V , and have the same value for different densities, although still show a variability with the rods diameter.

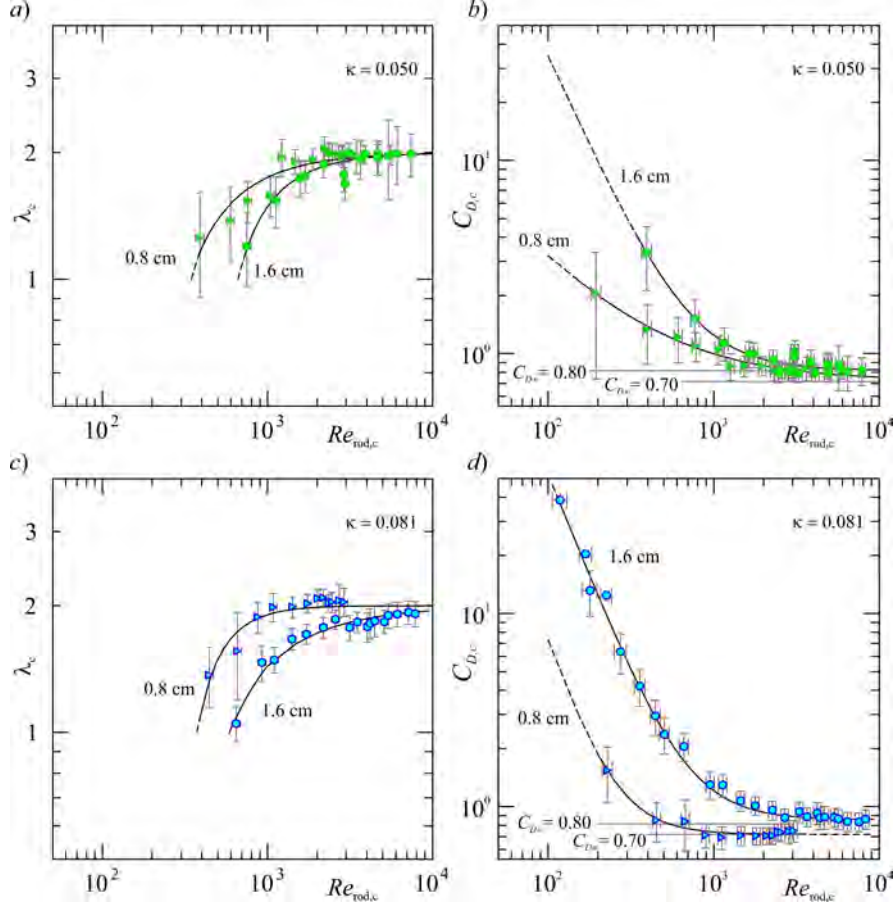


FIGURE A.5. Comparison of drag measurements for 1.6 and 0.8 cm diameter rods. *a)* Exponent λ_c and *b)* drag coefficient $C_{D,c} = 2F/(\rho AV_c^2)$ for $\kappa = 0.050$ as a function of $Re_{rod,c} = V_c D/\nu$; *c)* and *d)* same variables for $\kappa = 0.081$. Curves are the interpolating functions, error bars refer to one standard deviation. Subscript ‘c’ refers the variables to data elaboration with V_c instead of V .

B. Scaling rules of the system

Our goal is to develop dynamic similarity criteria that allow to relate two realizations of the physical process we are analysing, but with different values of the variables or parameters involved: a first realization can be an experiment in the laboratory (model), a second realization can be the corresponding real GC in the field (prototype). We will make use of Direct Analysis, with similarity criteria developed on the basis of the two equations (2.5-2.6) that govern the process (see Longo 2021).

Assuming a common vertical and radial geometric scale r_l (undistorted model), results

$$r_{g'} = r_c r_u^\lambda, \quad (\text{B.1a})$$

$$r_l^3 = r_q r_t^\alpha, \quad (\text{B.1b})$$

where $r_{(\dots)}$ is the ratio between the value of the variable in the model and in the

	$\lambda = 1$	$\lambda = 2$
r_u	$r_{g'} r_D^2 \frac{r^{2(1-\kappa)}}{r_\nu r_\kappa^2}$	$r_{g'}^{1/2} r_D^{1/2} \frac{r^{1/2(1-\kappa)}}{r_\kappa^{1/2}}$
r_q		$r_l^{(3-\alpha)} r_u^\alpha$
r_{Re}	$r_{g'} r_l \left(\frac{r_D r_{(1-\kappa)}}{r_\nu r_\kappa} \right)^2$	$\frac{r_{g'}^{1/2} r_l}{r_\nu^{1/2}} \left(\frac{r_D r_{(1-\kappa)}}{r_\nu r_\kappa} \right)^{1/2}$
$r_{Re_{rod}}$	$r_{g'} r_D \left(\frac{r_D r_{(1-\kappa)}}{r_\nu r_\kappa} \right)^2$	$\frac{r_{g'}^{1/2} r_D}{r_\nu^{1/2}} \left(\frac{r_D r_{(1-\kappa)}}{r_\nu r_\kappa} \right)^{1/2}$

 TABLE B.3. Similarity ratios computed for the two cases $\lambda = 1$ and $\lambda = 2$, undistorted model.

prototype:

$$r_{(\dots)} = \frac{(\dots)_m}{(\dots)_p}. \quad (\text{B.2})$$

The subscript ‘ m ’ and ‘ p ’ stand for model and prototype, respectively.

Using the scaling rules (A.15), eq.(B.1a) reduces to

$$\begin{cases} r_u = r_{g'} r_D^2 \frac{r^{2(1-\kappa)}}{r_\nu r_\kappa^2}, & \lambda = 1, \\ r_u^2 = r_{g'} r_D \frac{r^{(1-\kappa)}}{r_\kappa}, & \lambda = 2, \end{cases} \quad (\text{B.3})$$

In eq.(B.3b) a classical Froude similarity is achieved, where the geometric scale is related to the stem diameter.

Eq.(B.1b) becomes

$$r_q = r_l^{3-\alpha} r_u^\alpha. \quad (\text{B.4})$$

We have two equations in eight variables, represented by the scale ratios

$$r_u, r_q, r_l, r_{g'}, r_D, r_{(1-\kappa)}, r_\kappa, r_\nu, \quad (\text{B.5})$$

with 6 degrees of freedom: for instance fixing $r_l, r_{g'}, r_D, r_{(1-\kappa)}, r_\kappa, r_\nu$ we can estimate r_u, r_q and the scale ratios for all the derived variables. We can select the scale ratios almost arbitrarily, as long as the two realizations of the physical process both satisfy the basic assumptions (shallow water equation, Boussinesq hypothesis, etc.) and Re and Re_{rod} take values in the range of validity of those assumptions. Table B.3 lists the similarity rules computed for $\lambda = 1, 2$, undistorted model.

Since the GCs we are studying can be very large in plan, it can be advantageous to make geometrically distorted models with a vertical scale larger than the horizontal scale. For geometrically distorted models, defining r_{l_h} and $r_{l_v} = n r_{l_h}$ the horizontal and vertical length scales ratios, respectively, and n the distortion coefficient (in general

	$\lambda = 1$	$\lambda = 2$
r_{u_h}	$nr_{g'}r_D^2 \frac{r^{2(1-\kappa)}}{r_\nu r_\kappa^2}$	$n^{1/2}r_{g'}^{1/2}r_D^{1/2} \frac{r^{1/2(1-\kappa)}}{r_\kappa^{1/2}}$
r_{u_v}		nr_{u_h}
r_q		$n^{1-\alpha}r_{l_h}^3 r_\nu^\alpha$
r_{Re}	$n^2 r_{g'} r_{l_h} \left(\frac{r_D r^{(1-\kappa)}}{r_\nu r_\kappa} \right)^2$	$n^{3/2} \frac{r_{g'}^{1/2}}{r_\nu^{1/2}} r_{l_h} \left(\frac{r_D r^{(1-\kappa)}}{r_\nu r_\kappa} \right)^{1/2}$
$r_{Re_{rod}}$	$nr_{g'} r_D \left(\frac{r_D r^{(1-\kappa)}}{r_\nu r_\kappa} \right)^2$	$n^{1/2} \frac{r_{g'}^{1/2}}{r_\nu^{1/2}} r_D \left(\frac{r_D r^{(1-\kappa)}}{r_\nu r_\kappa} \right)^{1/2}$

TABLE B.4. Similarity ratios computed for the two cases $\lambda = 1$ and $\lambda = 2$, distorted model.

$n > 1$), eqs.(B.3) become

$$\begin{cases} r_{u_h} = nr_{g'}r_D^2 \frac{r^{2(1-\kappa)}}{r_\nu r_\kappa^2}, & \lambda = 1, \\ r_{u_h}^2 = nr_{g'}r_D \frac{r^{(1-\kappa)}}{r_\kappa}, & \lambda = 2, \end{cases} \quad (\text{B.6})$$

with r_{u_h} now representing the horizontal velocity scale ratio; eq.(B.4) becomes

$$r_q = nr_{l_h}^{3-\alpha} r_{u_h}^\alpha \quad (\text{B.7})$$

and the vertical velocity scale ratio is $r_{u_v} = nr_{u_h}$.

Table B.4 lists the similarity ratios computed for $\lambda = 1, 2$; there are seven degrees of freedom in selecting the scale ratios.

If we add the further constraint that the two processes have an equal Reynolds number of the current and an equal Reynolds number of the rods, that is $r_{Re} = r_{Re_{rod}} = 1$, results in $r_D = nr_{l_h}$ and $r_{u_h} = r_\nu/(nr_{l_h})$ and yields

$$\begin{cases} r_{g'} = \frac{r_\nu^2 r_\kappa^2}{n^4 r_{l_h}^3 r^{2(1-\kappa)}}, & \lambda = 1, \\ r_{g'} = \frac{r_\nu^2 r_\kappa}{n^4 r_{l_h}^3 r^{(1-\kappa)}}, & \lambda = 2. \end{cases} \quad (\text{B.8})$$

Table B.5 lists the similarity ratios computed for $\lambda = 1, 2$ by imposing the same values of Re in the two processes and the same Re_{rod} in the two processes; there are five degrees of freedom in selecting the scale ratios. In practical case, these similarity rules are too restrictive and essentially not necessary as long as, for instance, we have Re and Re_{rod} in the two processes to guarantee the same λ in the two processes.

	$\lambda = 1$	$\lambda = 2$
r_D		$n r_{l_h}$
r_{u_h}		$\frac{r_\nu}{n r_{l_h}}$
r_{u_v}		$\frac{r_\nu}{r_{l_h}}$
$r_{g'}$	$\frac{r_\nu^2 r_\kappa^2}{n^4 r_{l_h}^3 r_{(1-\kappa)}^2}$	$\frac{r_\nu^2 r_\kappa}{n^4 r_{l_h}^3 r_{(1-\kappa)}}$
r_q		$n^{1-\alpha} r_{l_h}^3 r_\nu^\alpha$
r_{Re}		1
$r_{Re_{rod}}$		1

TABLE B.5. Similarity ratios computed by imposing $r_{Re} = 1$ and $r_{Re_{rod}} = 1$ for the two cases $\lambda = 1$ and $\lambda = 2$, distorted model.

We note that large variations of r_κ are accompanied by small variations of $r_{(1-\kappa)}$ hence this last scale ratio can be assumed constant.

If we wish to extrapolate, e.g., Exp. 11 in our tank (model) to a prototype scale (real field), assuming $r_{l_h} = 1/20$, $n = 5$, $r_\kappa = r_{(1-\kappa)} = 1$, $r_\nu \approx 1$, $r_D = 4$ and $r_{g'} = 1/2$ and $\lambda = 2$, results $r_{u_h} = 3.16$, $r_{u_v} = 15.8$, $r_{Re} = 0.79$, $r_{Re_{rod}} = 12.6$. We refer to the rules listed in table B.4. The current is almost three times slower in the prototype than in the model, with Re larger in the prototype than in the model but with the Re_{rod} almost one tenth in the model than in the prototype. This last effect must be carefully checked in order to guarantee a sufficiently high value of Re_{rod} also in the prototype. The inflow rate in the prototype is almost 25 times the inflow rate in the model. In dimensional variables, Exp. 11 can be extrapolated to a real field GC of density $\rho_{c_p} \approx 1043 \text{ kg m}^{-3}$ advancing in water, released in the presence of vegetation with diameter $D_p = 0.4 \text{ cm}$ and with an inflow rate (referred to the full circle) $q'_p \approx 61 \text{ l s}^{-1}$. The experimental initial front speed was $u_{N_m} = 2.7 \text{ cm s}^{-1}$ in the model, resulting in $u_{N_p} \approx 0.85 \text{ cm s}^{-1}$ in the real field.

In practical situations, it may be necessary to reproduce a natural GC in the laboratory, to investigate certain aspects that may have escaped observation in the field, or to reconstruct measurements never made in the field, or to verify the consequences of accidents with environmental damages and possible pollution consequences. In these cases it is convenient to adopt the following rules:

- reduce the horizontal geometric scale, with $r_{l_h} \ll 1$ in order to contain the model in the space available in the laboratory;
- choose a vertical scale greater than the horizontal one, $n > 1$, in order to generate, in the laboratory, currents with a thickness that can be measured with adequate accuracy: $n < 10$ is also suggested to avoid an excessive distortion of the flow field;
- in order to reproduce the vegetation, select cylinders with an adequate diameter for the practical operations of laying, with $r_D > 1$;

- maintain a ratio $r_{g'} = \mathcal{O}(1)$ or slightly different, to facilitate the preparation of the fluid of the stream, using water as the ambient fluid;
- check that the required flow rate, with the chosen scale ratios, can be achieved with the pumps or the hydraulic circuit available in the laboratory;
- the selection of $r_\kappa, r_{(1-\kappa)}$ can be adapted to the needs, although it is advisable to have $r_\kappa = \mathcal{O}(1), r_{(1-\kappa)} = \mathcal{O}(1)$;
- check that Re and Re_{rod} are comparable in model and prototype. It may be convenient to increase the viscosity of the current fluid used in the experiments (e.g. by adding glycerol), with $r_\nu > 1$, to modulate the Reynolds numbers values.

Declaration of Interests

The authors report no conflict of interest.

Acknowledgements

The cost of the equipment used for this experimental investigation was partly supported by the University of Parma through the Scientific Instrumentation Upgrade Programme 2018. D. P. has been partly supported by the Programme ‘‘FIL 2019-Quota Incentivante’’ of University of Parma and co-sponsored by Fondazione Cariparma.

M. U. thanks the Dept. of Mechanical and Aerospace Engineering at Princeton University for supporting a visit in summer 2019 during which a part of this research was performed. We thank Prof. H. A. Stone for interesting discussions of the problem.

The authors thank the master degree student Nicolò Merli for his help in data acquisition and data analysis.

REFERENCES

- BELCHER, S. E., HARMAN, I. N. & FINNIGAN, J. J. 2012 The wind in the willows: flows in forest canopies in complex terrain. *Annual Review of Fluid Mechanics* **44**, 479–504.
- BENJAMIN, T. B. 1968 Gravity currents and related phenomena. *Journal of Fluid Mechanics* **31** (2), 209–248.
- CENEDESE, C., NOKES, R. & HYATT, J. 2018 Lock-exchange gravity currents over rough bottoms. *Environmental Fluid Mechanics* **18** (1), 59–73.
- CHIAPPONI, L., UNGARISH, M., LONGO, S., DI FEDERICO, V. & ADDONA, F. 2018 Critical regime of gravity currents flowing in non-rectangular channels with density stratification. *Journal of Fluid Mechanics* **840**, 579–612.
- CHIAPPONI, L., UNGARISH, M., PETROLO, D., DI FEDERICO, V. & LONGO, S. 2019 Non-boussinesq gravity currents and surface waves generated by lock release in a circular-section channel: theoretical and experimental investigation. *Journal of Fluid Mechanics* **869**, 610–633.
- CHOWDHURY, M. R. & TESTIK, F. Y. 2014 A review of gravity currents formed by submerged single-port discharges in inland and coastal waters. *Environmental Fluid Mechanics* **14** (2), 265–293.
- DE FALCO, M. C., ADDUCE, C., NEGRETTI, M. E. & HOPFINGER, E. J. 2021 On the dynamics of quasi-steady gravity currents flowing up a slope. *Advances in Water Resources* **147**, 103791.
- DI FEDERICO, V., ARCHETTI, R. & LONGO, S. 2012 Spreading of axisymmetric non-newtonian power-law gravity currents in porous media. *Journal of Non-Newtonian Fluid Mechanics* **189**, 31–39.
- DI FEDERICO, V., LONGO, S., KING, S. E., CHIAPPONI, L., PETROLO, D. & CIRIELLO, V. 2017 Gravity-driven flow of Herschel–Bulkley fluid in a fracture and in a 2d porous medium. *Journal of Fluid Mechanics* **821**, 59–84.

- ERGUN, S. 1952 Fluid flow through packed columns. *Chemical Engineering Progress* **48**, 89–94.
- FINNIGAN, J. 2000 Turbulence in plant canopies. *Annual Review of Fluid Mechanics* **32** (1), 519–571.
- HATCHER, L., HOGG, A. J. & WOODS, A. W. 2000 The effects of drag on turbulent gravity currents. *Journal of Fluid Mechanics* **416**, 297–314.
- HOGG, A. J., UNGARISH, M. & HUPPERT, H. E. 2000 Particle-driven gravity currents: asymptotic and box model solutions. *European Journal of Mechanics-B/Fluids* **19** (1), 139–165.
- HUPPERT, H. E. 2006 Gravity currents: a personal perspective. *Journal of Fluid Mechanics* **554**, 299.
- LANE-SERFF, G. F. 1993 On drag-limited gravity currents. *Deep Sea Research Part I: Oceanographic Research Papers* **40** (8), 1699–1702.
- LAUBER, G. & HAGER, W. H. 1998 Experiments to dambreak wave: Horizontal channel. *Journal of Hydraulic Research* **36** (3), 291–307.
- LIPPERT, M. C. & WOODS, A. W. 2020 Experiments on the sedimentation front in steady particle-driven gravity currents. *Journal of Fluid Mechanics* **889**.
- LONGO, S. 2021 *Principles and Applications of Dimensional Analysis and Similarity*. Springer.
- LONGO, S., UNGARISH, M., DI FEDERICO, V., CHIAPPONI, L. & ADDONA, F. 2016 Gravity currents in a linearly stratified ambient fluid created by lock release and influx in semi-circular and rectangular channels. *Physics of Fluids* **28** (9), 096602.
- LONGO, S., UNGARISH, M., DI FEDERICO, V., CHIAPPONI, L. & MARANZONI, A. 2015 The propagation of gravity currents in a circular cross-section channel: experiments and theory. *Journal of Fluid Mechanics* **764**, 513.
- LONGO, S., UNGARISH, M., DI FEDERICO, V., CHIAPPONI, L. & PETROLO, D. 2018 Gravity currents produced by lock-release: theory and experiments concerning the effect of a free top in non-boussinesq systems. *Advances in Water Resources* **121**, 456–471.
- MACDONALD, I. F., EL-SAYED, M. S., MOW, K. & DULLIEN, F. A. L. 1979 Flow through porous media—the ergun equation revisited. *Industrial & Engineering Chemistry Fundamentals* **18** (3), 199–208.
- MARTIN, A., NEGRETTI, M. E., UNGARISH, M. & ZEMACH, T. 2020 Propagation of a continuously supplied gravity current head down bottom slopes. *Physical Review Fluids* **5** (5), 054801.
- MAXWORTHY, T. 1983 Gravity currents with variable inflow. *Journal of Fluid Mechanics* **128**, 247–257.
- NAFTCHALI, A. K., KHOZEYMEHNEZHAD, H., AKBARPOUR, A. & VARJAVAND, P. 2016 Experimental study on the effects of artificial vegetation density on forehead of saline current flow. *Ain Shams Engineering Journal* **7** (2), 799–809.
- NEPF, H. M. 2012 Flow and transport in regions with aquatic vegetation. *Annual Review of Fluid Mechanics* **44**, 123–142.
- OTTOLENGHI, L., ADDUCE, C., INGHILESI, R., ROMAN, F. & ARMENIO, V. 2016 Mixing in lock-release gravity currents propagating up a slope. *Physics of Fluids* **28** (5), 056604.
- OZAN, A. Y., CONSTANTINESCU, G. & HOGG, A. J. 2015 Lock-exchange gravity currents propagating in a channel containing an array of obstacles. *Journal of Fluid Mechanics* **765**, 544–575.
- SAYAG, R. & WORSTER, G. M. 2013 Axisymmetric gravity currents of power-law fluids over a rigid horizontal surface. *Journal of Fluid Mechanics* **716**, R5.
- SCIORTINO, G., ADDUCE, C. & LOMBARDI, V. 2018 A new front condition for non-boussinesq gravity currents. *Journal of Hydraulic Research* **56** (4), 517–525.
- SHER, D. & WOODS, A. W. 2017 Mixing in continuous gravity currents. *Journal of Fluid Mechanics* **818**.
- SIMPSON, J. E. 1999 *Gravity currents: In the environment and the laboratory*. Cambridge University Press.
- SPARKS, R. S. J., BONNECAZE, R. T., HUPPERT, H. E., LISTER, J. R., HALLWORTH, M. A., MADER, H. & PHILLIPS, J. 1993 Sediment-laden gravity currents with reversing buoyancy. *Earth and Planetary Science Letters* **114** (2-3), 243–257.
- STONE, B. M. & SHEN, H. T. 2002 Hydraulic resistance of flow in channels with cylindrical roughness. *Journal of Hydraulic Engineering* **128** (5), 500–506.

- TANINO, Y., NEPF, H. M. & KULIS, P. S. 2005 Gravity currents in aquatic canopies. *Water Resources Research* **41** (12).
- TESTIK, F. Y. & UNGARISH, M. 2016 On the self-similar propagation of gravity currents through an array of emergent vegetation-like obstacles. *Physics of Fluids* **28** (5), 056605.
- TESTIK, F. Y. & YILMAZ, N. A. 2015 Anatomy and propagation dynamics of continuous-flux release bottom gravity currents through emergent aquatic vegetation. *Physics of Fluids* **27** (5), 056603.
- TSAKIRI, M., PRINOS, P. & KOFTIS, T. 2016 Numerical simulation of turbulent exchange flow in aquatic canopies. *Journal of Hydraulic Research* **54** (2), 131–144.
- UNGARISH, M. 2009 *An introduction to gravity currents and intrusions*. CRC press.
- UNGARISH, M. 2018 Thin-layer models for gravity currents in channels of general cross-section area, a review. *Environmental Fluid Mechanics* **18** (1), 283–333.
- UNGARISH, M. 2020 *Gravity Currents and Intrusions*. World Scientific.
- VARGAS-LUNA, A., CROSATO, A., CALVANI, G. & UIJTTEWAAL, W. S. J. 2016 Representing plants as rigid cylinders in experiments and models. *Advances in Water Resources* **93**, 205–222.
- WHITAKER, S. 1996 The Forchheimer equation: a theoretical development. *Transport in Porous Media* **25** (1), 27–61.
- ZEMACH, T., CHIAPPONI, L., PETROLO, D., UNGARISH, M., LONGO, S. & DI FEDERICO, V. 2017 On the propagation of particulate gravity currents in circular and semi-circular channels partially filled with homogeneous or stratified ambient fluid. *Physics of Fluids* **29** (10), 106605.
- ZGHEIB, N., BONOMETTI, T. & BALACHANDAR, S. 2015 Dynamics of non-circular finite release gravity currents. *Journal of Fluid Mechanics* **783**, pp-344.
- ZHANG, X. & NEPF, H. M. 2008 Density-driven exchange flow between open water and an aquatic canopy. *Water Resources Research* **44** (8).